

AD-A039 771

SYSTEMS SCIENCE AND SOFTWARE LA JOLLA CALIF  
HYBRID EM METHODS.(U)

F/G 9/3

MAY 77 I KATZ, D E PARKS, A WILSON

F29601-76-C-0025

UNCLASSIFIED

SSS-R-76-2976

AFWL-TR-76-266

NL

1 of 1  
ADA039 771



AFWL-TR-76-266

AFWL-TR-  
76-266

AD A 039771



## HYBRID EM METHODS

Systems, Science and Software  
La Jolla, CA 92038

May 1977

Final Report



Approved for public release; distribution unlimited.

AIR FORCE WEAPONS LABORATORY  
Air Force Systems Command  
Kirtland Air Force Base, NM 87117

DDC FILE COPY

This final report was prepared by Systems, Science and Software, La Jolla, California, under Contract F29601-76-C-0025, Job Order 46950331 with the Air Force Weapons Laboratory, Kirtland Air Force Base, New Mexico. Mr. William D. Bell (DYC) was the Laboratory Project Officer-in-Charge.

When US Government drawings, specifications, or other data are used for any purpose other than a definitely related Government procurement operation, the Government thereby incurs no responsibility nor any obligation whatsoever, and the fact that the Government may have formulated, furnished, or in any way supplied the said drawings, specifications, or other data is not to be regarded by implication or otherwise as in any manner licensing the holder or any other person or corporation or conveying any rights or permission to manufacture, use, or sell any patented invention that may in any way be related thereto.

This report has been reviewed by the Office of Information (OI) and is releasable to the National Technical Information Service (NTIS). At NTIS, it will be available to the general public, including foreign nations.

This technical report has been reviewed and is approved for publication.

*William D Bell*

WILLIAM D. BELL  
Project Officer

FOR THE COMMANDER

*Miles T. Barnett, Jr.*  
MILES T. BARNETT, JR.  
Major, USAF  
Chief, Satellite and C<sup>3</sup> Branch

*Paul J. Daily*  
PAUL J. DAILY  
Colonel, USAF  
Chief, Technology & Analysis Division



DO NOT RETURN THIS COPY. RETAIN OR DESTROY.

UNCLASSIFIED

SECURITY CLASSIFICATION OF THIS PAGE (When Data Entered)

| REPORT DOCUMENTATION PAGE  |   | READ INSTRUCTIONS<br>BEFORE COMPLETING FORM |
|--|---|---|
| 1. REPORT NUMBER<br>18 AFWL-TR-76-266 ✓  | 2. GOVT ACCESSION NO.   | 3. RECIPIENT'S CATALOG NUMBER               |
| 4. TITLE (and Subtitle)<br>6 HYBRID EM METHODS ✓   | 5. TYPE OF REPORT & PERIOD COVERED<br>9 Final Report                                    |   |
| 7. AUTHOR(s)<br>10 Ira Katz, Donald E. Parks, Andrew Wilson,<br>James M. Harvey, Manuel Rotenberg  | 14 PERFORMING ORG. REPORT NUMBER<br>SSS-R-76-2976                                       |   |
| 9. PERFORMING ORGANIZATION NAME AND ADDRESS<br>Systems, Science and Software<br>La Jolla, California 92038   | 8. CONTRACT OR GRANT NUMBER(s)<br>15 F29601-76-C-0025 new                               |   |
| 11. CONTROLLING OFFICE NAME AND ADDRESS<br>Air Force Weapons Laboratory (DYC)<br>Kirtland Air Force Base, NM 87117   | 10. PROGRAM ELEMENT, PROJECT, TASK<br>AREA & WORK UNIT NUMBERS<br>64711F/46950331 17 03 |   |
| 14. MONITORING AGENCY NAME & ADDRESS (if different from Controlling Office)  | 12. REPORT DATE<br>1 May 1977   |   |
|  | 13. NUMBER OF PAGES<br>76 12 72 pgs   |   |
|  | 15. SECURITY CLASS. (of this report)<br>UNCLASSIFIED                                    |   |
| 15a. DECLASSIFICATION/DOWNGRADING<br>SCHEDULE  |   |   |
| 16. DISTRIBUTION STATEMENT (of this Report)<br><br>Approved for public release; distribution unlimited.  |   |   |
| 17. DISTRIBUTION STATEMENT (of the abstract entered in Block 20, if different from Report)   |   |   |
| 18. SUPPLEMENTARY NOTES  |   |   |
| 19. KEY WORDS (Continue on reverse side if necessary and identify by block number)<br>SGEMP<br>Particle Codes<br>Surface Currents<br>Hybrid Codes<br>Boundary Conditions<br>Struts   |   |   |
| 20. ABSTRACT (Continue on reverse side if necessary and identify by block number)<br>This report summarizes a study of hybrid electrostatic-electromagnetic techniques for the calculation of SGEMP generated surface currents. Presented are results using the hybrid SQUID code, a technique to treat the currents in small struts, and a theory of nonreflective boundary conditions for electromagnetic SGEMP codes. |   |   |



## TABLE OF CONTENTS

| <u>SECTION</u>   | <u>Page</u> |
|--|-------------|
| I INTRODUCTION. . . . .  | 5           |
| II SGEMP RESPONSE CALCULATIONS USING THE SQUID<br>HYBRID EM CODE. . . . .                                | 6           |
| 2.1 Theoretical Basis of the Hybrid SQUID Code . . . . .   | 6           |
| 2.1.1 The Purpose of SQUID. . . . .  | 6           |
| 2.1.2 SQUID Centering Scheme. . . . .  | 9           |
| 2.1.3 SQUID Dipole Correct Current<br>Algorithm . . . . .  | 11          |
| 2.1.4 Correcting the Local Longitudinal<br>Field . . . . .   | 14          |
| 2.2 Hybrid EM Calculations . . . . .   | 19          |
| 2.3 Discussion of Results. . . . .   | 26          |
| III A TECHNIQUE FOR TREATING SMALL CURRENT CARRYING<br>STRUTS IN ELECTROMAGNETIC PARTICLE CODES. . . . . | 32          |
| 3.1 Fields Near a Strut. . . . .   | 33          |
| 3.2 3-D Difference Equations . . . . .   | 35          |
| 3.3 Linear Strut in a 3-D Geometry . . . . .   | 38          |
| 3.4 Two-Dimensional Simulations of Strut<br>Geometry . . . . .   | 41          |
| 3.5 Test Calculations. . . . .   | 44          |
| 3.6 Conclusions. . . . .   | 58          |
| IV NONREFLECTIVE FREE SPACE BOUNDARY CONDITIONS<br>FOR SGEMP CODES . . . . .                             | 59          |
| 4.1 Analytical Results . . . . .   | 63          |
| 4.2 1-D Parameter Study. . . . .   | 68          |
| 4.3 Damped Wave Boundaries in Two Dimensions . . . . .   | 72          |

## ILLUSTRATIONS

| <u>Figure</u> |  | <u>Page</u> |
|---------------|--|-------------|
| 1             | Exposure object and points of interest. . . . .  | 7           |
| 2             | Conventional centering in two-dimensional<br>electromagnetic code. . . . .   | 10          |
| 3             | Modified centering. . . . .  | 10          |
| 4             | A single particle a distance $x$ above the surface.  | 12          |
| 5             | The surface electric field for a charge sheet a<br>distance $x$ above the conducting surface . . . . .   | 15          |
| 6             | The grid for the high fluence SGEMP problem . . . . .  | 18          |
| 7             | The calculational grid. . . . .  | 20          |
| 8             | Midplane surface currents as a function of time . . . . .  | 22          |
| 9             | The surface current at point C in amperes per m . . . . .  | 24          |
| 10            | The surface currents in amperes per meter at<br>point E for the three different rod diameters . . . . .  | 25          |
| 11            | The perpendicular component of the electric<br>field as a function of distance from the surface<br>3 nanoseconds into the calculation. . . . .     | 28          |
| 12            | The electron sheath 3 nanoseconds into the problem.  | 29          |
| 13            | 3-D strut calculation . . . . .  | 36          |
| 14            | The configuration used for testing the response<br>of loaded struts. . . . .   | 45          |
| 15            | Strut current vs. time for an induction per unit<br>length of $5 \times 10^{-21} \text{ sec}^2/\text{cm}^2$ . . . . .                              | 47          |
| 16            | Strut current vs. time for an inductance per unit<br>length of $3.125 \times 10^{-22} \text{ sec}^2/\text{cm}^2$ . . . . .                         | 49          |
| 17            | Strut current vs. time for an inductance per unit<br>length of $5 \times 10^{-21} \text{ sec}^2/\text{cm}^2$ and no strut<br>capacitance . . . . . | 50          |
| 18            | Electric fields in the example without capacitance.  | 51          |
| 19            | Electric fields in the case with capacitance. . . . .  | 52          |

## ILLUSTRATIONS

| <u>Figure</u> |   | <u>Page</u> |
|---------------|---|-------------|
| 20            | The configuration used for testing the response of isolated struts. . . . .                     | 54          |
| 21            | Current on an isolated 120 cm strut . . . . .   | 55          |
| 22            | Current on a 120 cm isolated strut. . . . .   | 56          |
| 23            | Current on an isolated 160 cm strut . . . . .   | 57          |
| 24            | Remaining field amplitude vs. frequency for the 1-dimension parameter study . . . . .           | 71          |
| 25            | The configuration used for testing the effectiveness of the damping in two-dimensions . . . . . | 73          |
| 26            | The current at the wire center vs. time for the case with no damping. . . . .                   | 74          |
| 27            | The current at the wire center vs. time with damping in the outermost 5 zones. . . . .          | 75          |

## SECTION I

### INTRODUCTION

This final report summarizes a study of hybrid electrostatic-electromagnetic techniques for the calculation of surface currents caused by the motion of photoelectrons emitted from satellites. Section II presents the results using the hybrid SQUID code for a series of SGEMP test cases. Section III describes a technique to treat currents in small struts and presents some calculations using this technique. Section IV presents the theory of nonreflective boundary conditions for electromagnetic SGEMP codes. Included are one- and two-dimensional calculations showing the effectiveness of the boundary conditions in preventing the reflection of outgoing electromagnetic waves.



## SECTION II

### SGEMP RESPONSE CALCULATIONS USING THE SQUID HYBRID EM CODE

A series of SGEMP response calculations was performed using the hybrid SQUID code on the configuration shown in Figure 1. The diameter of the support varied between zero and 10 cm. This simple axisymmetric configuration is similar to that of a proposed SGEMP experiment. Our purpose was to examine the efficiency of a hybrid calculational technique, SQUID, for determining SGEMP response. The SQUID technique treats heavily space charge limited behavior close to emitting surfaces with high resolution. It calculates dipole correct electromagnetic response for far field effects while including correct monopole electric fields and particle trajectories near emitting surfaces.

In Section 2.1 of this report we discuss, in detail, the SQUID theory. The particular calculations performed are described in Section 2.2. Finally, we discuss the numerical results and their implications to future SGEMP response calculations in Section 2.3.

#### 2.1 THEORETICAL BASIS OF THE HYBRID SQUID CODE

##### 2.1.1 The Purpose of SQUID

The reader should be familiar with the basic techniques of fully electromagnetic (EM) particle codes, which have been fully described elsewhere (References 1, 2). This discussion

1. Boris, J. P., "Relativistic Plasma Simulation-Optimization of a Hybrid Code," Proc. 4th Conf. on Numerical Simulation of Plasmas, pp. 3-67, NRL, Washington, D.C., November 1970.
2. Katz, Ira, James Harvey and Andrew Wilson, "Particle Simulation Techniques for SGEMP," Systems, Science and Software Report SSS-R-75-2604, July 1975.

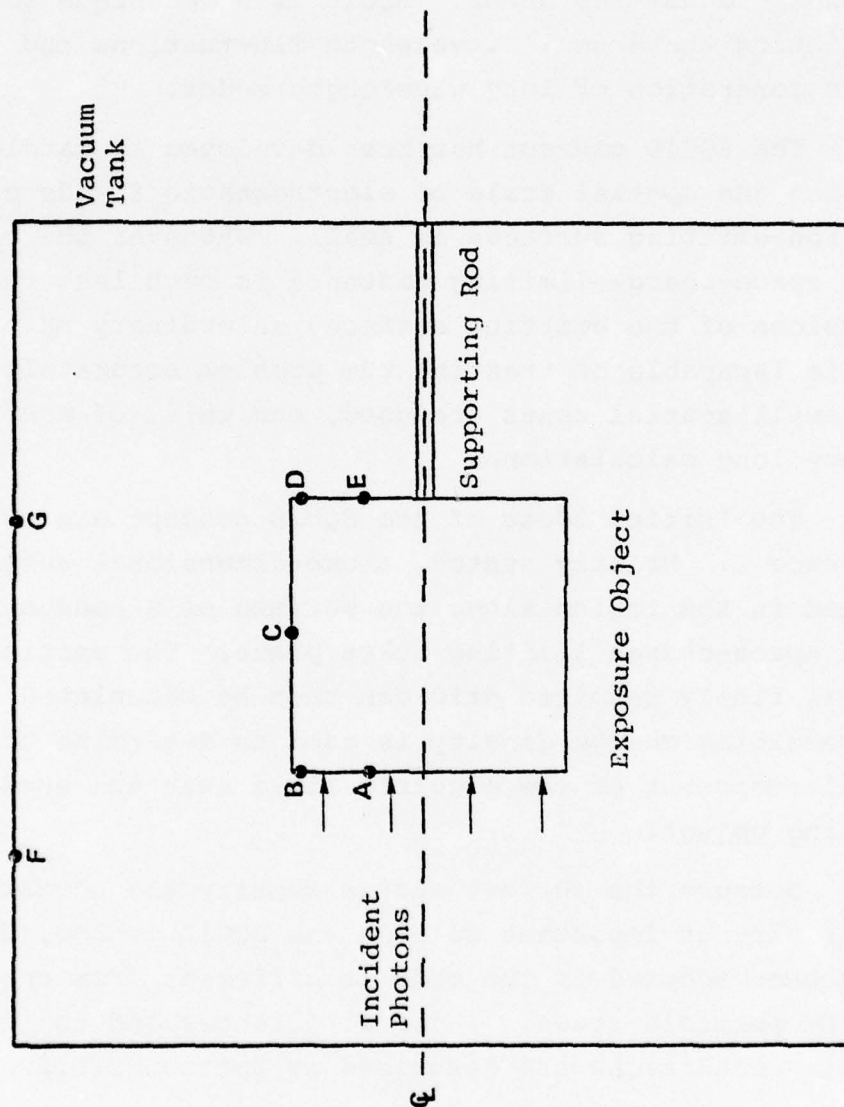


Figure 1 - Exposure object and points of interest.

emphasizes the differences between SQUID techniques and the usual particle code algorithms. It is in the neighborhood of object boundaries that rapid variations in field strengths and charge densities occur. SQUID is a technique for accurately calculating these small wavelength fluctuations and their effect on the generation of long wavelength modes.

The SQUID concept has been developed to handle problems in which the spatial scale of electrostatic fields close to electron-emitting surfaces is small. Whenever the characteristic space-charge limiting distance is much less than the dimensions of the emitting surface, an ordinary EM particle code is incapable of treating the problem accurately unless very small spatial zones are used, and this, of course, leads to very long calculations.

The initial ideas of the SQUID concept are outlined in Reference 2. Briefly stated, a one-dimensional subgrid is defined in the region along the surface of a conducting object where space-charge limiting takes place. The particle dynamics in this finely resolved grid can then be calculated accurately. The resulting charge density is used to determine the screened normal component of the electric field near the surface of the emitting object.

Because the surface charge density and normal electric fields play an important role in the SQUID method, the centering scheme adopted in the code is different from that of ordinary EM particle codes. These differences and the treatment of boundary conditions are described in Section 2.1.2.

Some care must be exercised in distributing the charge of a particle among adjacent cells in order that the charge dipoles set up along boundaries by moving particles are accurately calculated. Currents on the surface can be generated by EM wave interactions. In Section 2.1.3, we describe an algorithm to calculate particle currents so that transverse EM waves generated by these individual particles will be calculated correct to dipole order.

In Section 2.1.4, we describe how physically meaningful longitudinal electric fields can be calculated with subgrid resolution in those cases where the transverse fields have wavelengths long compared with cell dimensions, but where significant charge density fluctuations occur near the surface on a scale length small compared with cell dimensions.

### 2.1.2 SQUID Centering Scheme

Conducting boundary conditions on the electromagnetic fields in particle codes are easily applied; the tangential electric field is forced to be zero. In the ordinary centering of particle code grids, conducting physical boundaries pass through points where the tangential electric fields are defined as in Figure 2. Since the boundary conditions are applied directly, this formulation is extremely convenient to apply and is most commonly used. However, some quantities relevant to surface phenomena, such as surface charges, are not directly accessible and, indeed, must be extrapolated from interior values. In dealing with the effects of photon generated electrons on metallic objects, the surface response is the desired information. Consequently, we have adapted a modified centering scheme as shown in Figure 3 where normal electric fields and tangential magnetic fields are defined directly on the surface. This enables one to calculate surface charges and skin currents directly. The boundary condition on the tangential electric field is

$$E_{||}(\text{below surface}) = -E_{||}(\text{above surface})$$

Since all our field equations are advanced using a first-order symmetric difference form, this boundary condition is entirely equivalent to

$$E_{||}(\text{surface}) = 0 = \frac{1}{2} [E_{||}(\text{below surface}) + E_{||}(\text{above surface})]$$



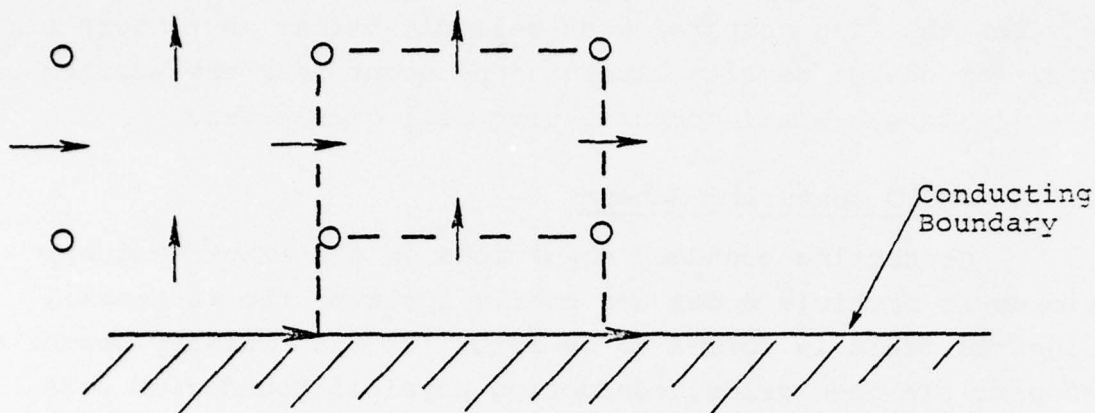


Figure 2 - Conventional centering in two-dimensional electromagnetic code.

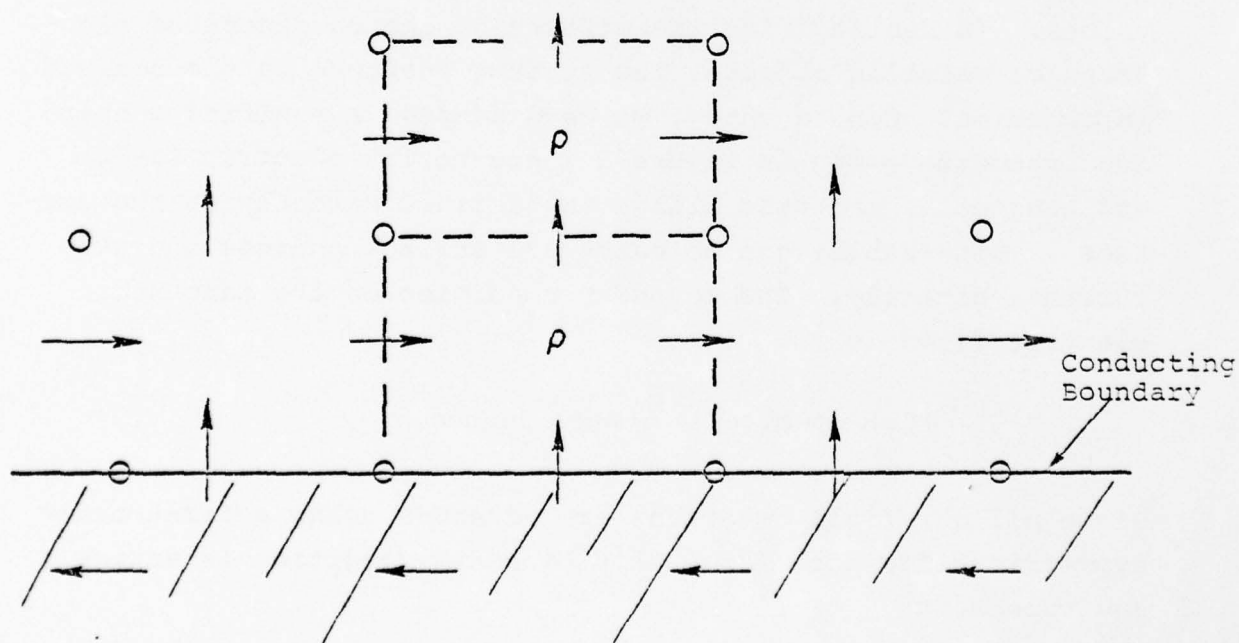


Figure 3 - Modified centering.

### 2.1.3 SQUID Dipole Correct Current Algorithm

For purposes of numerical smoothing, finite-sized particles are frequently used in EM particle codes. However, the literal interpretation of a particle as a charge smeared over a finite region is fraught with danger in problems where boundaries play an important role. In cases where limiting occurs within a single cell, this interpretation can lead to incorrect results when the dipole field (resulting from the motion of charge away from a surface) is being calculated.

Instead of regarding a particle as a finite-sized object which is pushed according to appropriate area weights of the electric fields in its vicinity, we prefer to consider the particle as located at a point in space and to push it by the interpolated field at that point. The difference in interpretation is merely semantic except near boundaries. There, the normal area-weighted treatment must be reconsidered.

While a particle is considered localized at a point for dynamical purposes, its charge density must be interpolated between adjacent cells because the charge density is evaluated at specified points in the grid, namely, at cell centers (see Figure 3). Near boundaries, special care has to be given to this interpolation in order that the current calculated gives rise to the correct electromagnetic field.

If a charge  $q$  moves a perpendicular distance  $x$  from a conducting surface, a distant observer sees a dipole field corresponding to a dipole of strength

$$d = 2 qx$$

The modified centering scheme in Figure 3 corresponds to cell centered charge densities. First examine the case of a particle at  $x$  between  $L/2$  and  $3L/2$  from the surface as shown in Figure 4. If this is the only charge in the system,

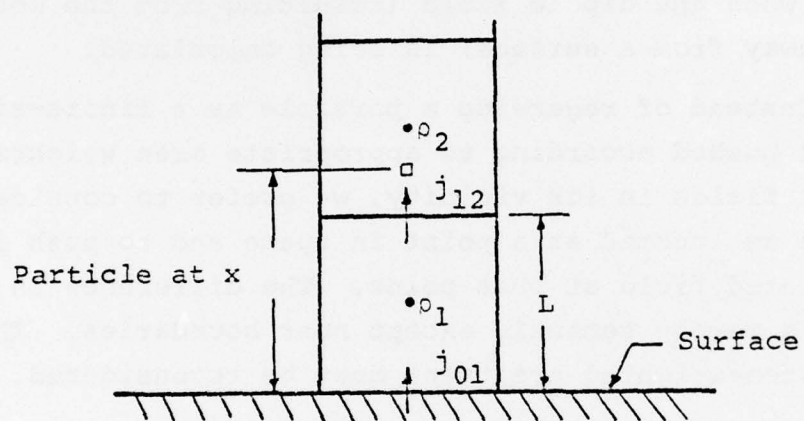


Figure 4 - A single particle a distance  $x$  above the surface.

then two equations are needed to get the correct dipole strength;

$$q = \rho_1 + \rho_2$$

$$2 qx = 2 \rho_1 (L/2) + 2 \rho_2 (3L/2)$$

Solving for  $\rho_1$  and  $\rho_2$ , find

$$\rho_1 = q \left( 1 - \frac{x - L/2}{L} \right)$$

$$\rho_2 = q \left( \frac{x - L/2}{L} \right)$$

Thus, the correct finite difference current  $j$  is just

$$j_{12} = \begin{cases} qv & L/2 < x < 3L/2 \\ 0 & \text{all other } x \end{cases}$$

For  $0 < x < L/2$ , there are not enough unknowns ( $\rho_2 = 0$ ) and in order to satisfy the distant observer, retain only the dipole equation

$$2 qx = 2 \rho_1 (L/2)$$

getting

$$j_{01} = \begin{cases} 2 qv & 0 < x < L/2 \\ 0 & \text{all other } x \end{cases}$$



One can visualize these dipole correct currents as resulting from finite size CIC particles of charge  $q$  centered at  $x$  along with image particles of charge  $q$  centered at  $-x$ . As it nears the surface, both the particle and its image contribute to the surface normal current  $j_{01}$ . This enables one to easily calculate currents for any velocity orientation which will correspond to the correct dipole moment to a distant observer. The variation in this dipole strength generates transverse electromagnetic waves.

#### 2.1.4 Correcting the Local Longitudinal Field

In the previous section, we dealt with the distant field strength which for a single emitted charge is dipolar in nature. However, the dominant field felt by the test charge is the monopole attraction from its image. In the one-dimensional case, the field on a test sheet is constant once the charge leaves the surface and the field on the surface rises immediately to the same constant as shown in Figure 5. However, the current algorithm described in Section 2.1.3 gives a surface field that rises linearly until the charge sheet is half a cell out from the surface. This is clearly an unphysical result when describing subgrid variations in charge density. Below, a technique is discussed for constructing the appropriate longitudinal electric field in the vicinity of the surface assuming that the charge density varies much more slowly parallel to the surface than in the normal direction.

The charge density,  $\sigma$ , on a surface zone can be expressed as the sum of time integrals of the skin current  $k$  and perpendicular particle current  $j$ ,

$$\sigma = - \int dt (\nabla_{\parallel} \cdot k + \nabla_{\perp} \cdot j)$$

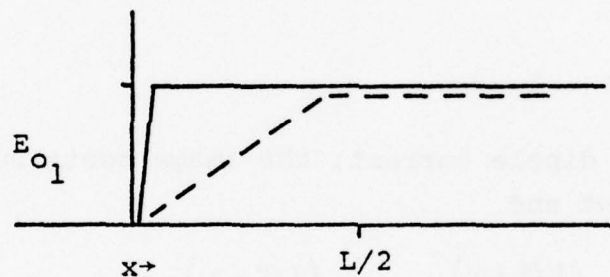


Figure 5 - The surface electric field for a charge sheet a distance  $x$  above the conducting surface. The solid line is the physical field, the dashed line is that generated using the dipole consistent current described in Section 2.1.

If the dipole correct current discussed in Section 2.1 is used, the surface charge reflects both the linear turn-on of the surface electric field and the partial tangential current canceling due to the image current.

$$\sigma_{\text{dipole}} = -\int (\nabla_{\parallel} \cdot \mathbf{k}_{\text{dipole}} + \nabla_{\perp} \cdot \mathbf{j}_{\text{dipole}}) dt$$

It is simple to calculate in the code the actual particle current leaving the surface. The image charge contribution to the surface current may be calculated in the following manner. If a particle of charge  $q$  is a distance  $0 < x < L/2$  from the surface, its contribution to the parallel current (real) is

$$j_{\parallel} = qv_{\parallel}$$

However, for the dipole current, the image contribution is included in the current and

$$j_{\parallel}^{\text{dipole}} = \underbrace{\left( \frac{L/2 + x}{L} \right) qv}_{\text{particle}} + \underbrace{\left( \frac{L/2 - x}{L} \right) (-q)v_{\parallel}}_{\text{image}}$$

Therefore, in order to find the true (monopole) charge density on a surface, include the complete image particle current

$$j_{\parallel} (\text{image}) = (-q)v_{\parallel}$$

in the skin current  $k$ . Assuming that the contributions to the surface charge from particles more than one cell away are the same in both monopole and dipole approximations, then

$$\sigma_{\text{monopole}} = \sigma_{\text{dipole}} + \int_0^t \left[ \nabla_{\perp} \cdot (j_{\text{monopole}} - j_{\text{dipole}}) + \nabla_{\parallel} \cdot (k_{\text{monopole}} - k_{\text{dipole}}) \right] dt$$

Knowing  $\sigma_{\text{monopole}}$ , the true surface electric field can be found. Spatial variation of the monopole electric field normal to the surface can easily be approximated if

$$\left| \frac{\partial \rho}{\partial x_{\parallel}} \right| \ll \left| \frac{\partial \rho}{\partial x_{\perp}} \right|$$

by a simple integral

$$E_{\perp}(x) = E_{\perp}(0) + \int_0^x \rho(\xi) d\xi$$

This equation is the basis of the SQUID subgrid screening approximation.

In practice, a pseudo-one-dimensional charge density is calculated for cells adjacent to emitting surfaces as shown in Figure 6. These charge densities are then used to give a screened normal component of the electric field which accelerates the particles.

$$\xi^t(x_{\perp}) = E_{\perp \text{ surface}}^t + \int_0^{x_{\perp}} \rho^t(x'_{\perp}) dx'_{\perp}$$

$$v_{\parallel}^{t+1/2} = v_{\parallel}^{t-1/2} + \Delta t(e/m) E_{\parallel}^t$$

$$v_{\perp}^{t+1/2} = v_{\perp}^{t-1/2} + \Delta t(e/m) \xi^t(x_{\perp})$$



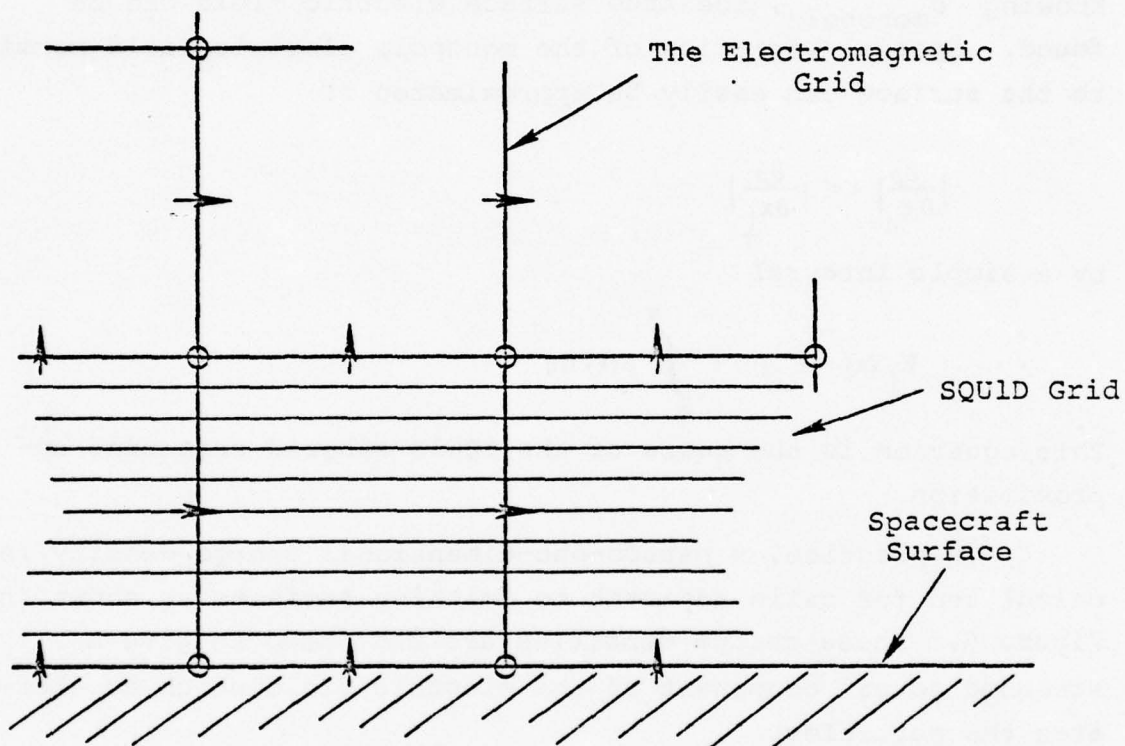


Figure 6 - The grid for the high fluence SGEMP problem. Each cell adjacent to a boundary,  $n$ , contains an entire quasi-one-dimensional grid. Associated with each SQUID grid is a one-dimensional charge density  $\rho_n(x_1)$  used for calculating the normal component of the electric field within the cell adjacent to the spacecraft surface.

As a result, the electrostatic field in the limiting sheath region is resolved in great detail in the direction normal to the surface, the direction in which it varies most rapidly.

## 2.2 HYBRID EM CALCULATIONS

Calculations of the response of an isolated cylinder to photogenerated electron emission have been performed in accordance with Task 1 (Section 4.1) of the Work Statement using the SQUID code.

For the sequence of calculations, a regular mesh with equal spacings of 10 cm in the  $r$  and  $z$  directions was employed for electromagnetic purposes. The five normal emission zones were subdivided, in accordance with the SQUID formulation, into 0.5-cm regions. The appearance of the gridded problem is shown in Figure 7.

Electron emission was accomplished through the use of seven energy bins. The angular distribution  $f(\theta, \phi)$  was  $\cos\theta$  in the normal direction and uniform in the polar angle  $\phi$ . The bin structure is as follows:

| <u>Bin</u> | <u>Fractional<br/>fluence</u> | <u>Energy (keV)</u> | <u>Velocity (in units of<br/>10 keV velocity)</u> |
|------------|-------------------------------|---------------------|---|
| 1          | 0.20028                       | 2.79                | 0.50758   |
| 2          | 0.24054                       | 7.43                | 0.86174   |
| 3          | 0.21810                       | 12.44               | 1.1139  |
| 4          | 0.16546                       | 17.34               | 1.3157  |
| 5          | 0.96678                       | 22.21               | 1.4896  |
| 6          | 0.7181                        | 29.79               | 1.7227  |
| 7          | 0.00713                       | 45.94               | 2.1398  |

The bin selection was strictly random for each particle in most runs, but in the final series, conditional selection was employed to guarantee that an equal number from each bin

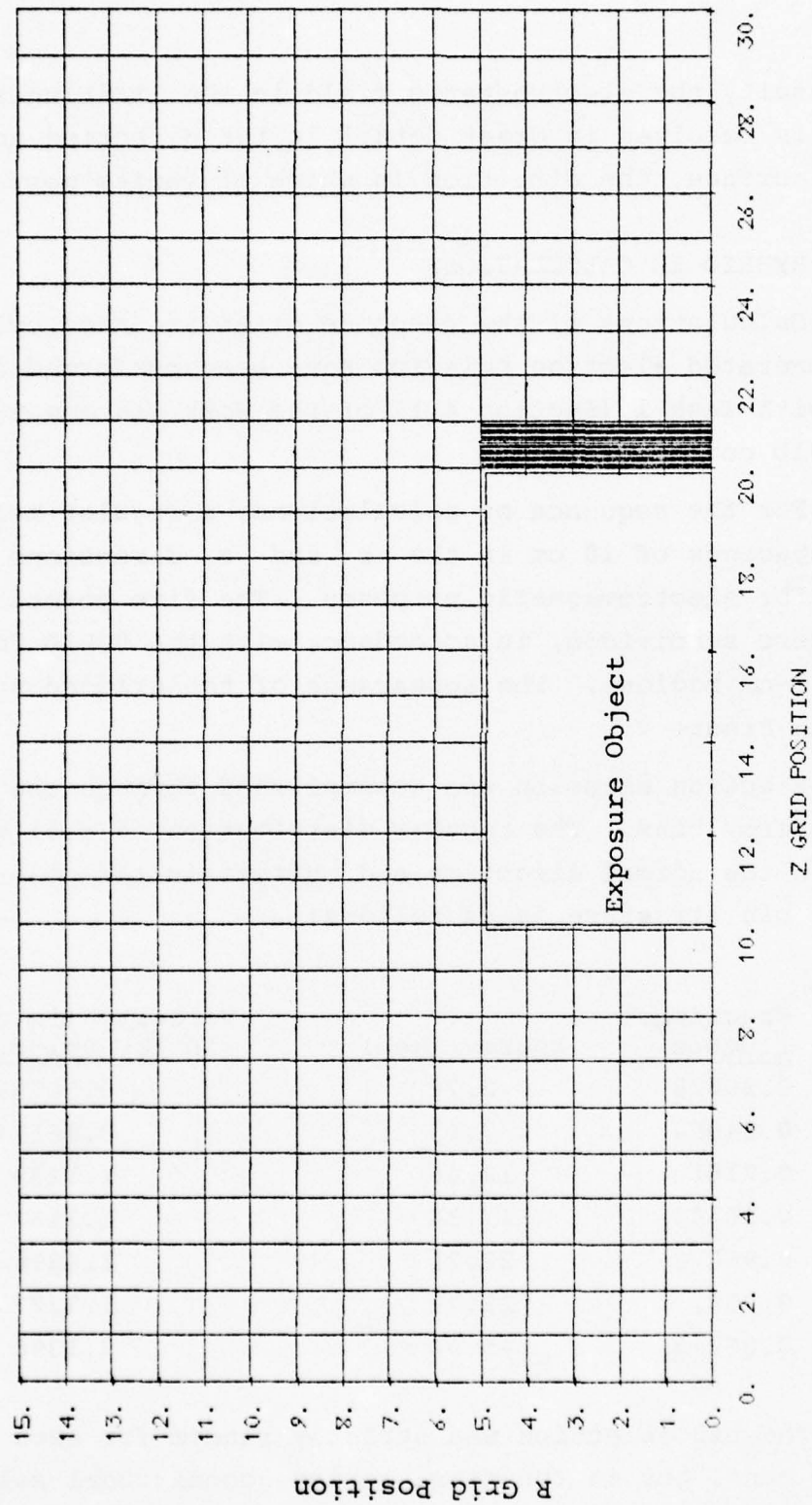


Figure 7 - The calculational grid.

was chosen each cycle. The emission was uniformly spaced in  $r$  along the surface. The pulse shape was given by a triangle with rise time of  $2.5 \times 10^{-9}$  sec with a peak current of  $7.88 \text{ amp/cm}^2$ .

The major parameter variations among the completed runs have been the number of particles emitted per cycle, the method of bin selection and the time step. Benchmark results were obtained using

$$\Delta t = 5 \times 10^{-11} \text{ sec}$$

$$\text{emission} = 300 \text{ particles/cycle}$$

This calculation had, on occasions, over 6000 particles within the grid, and the 200 cycles were required to go out to 10 ns. Total Central Processor Unit (CPU) time for the run, and a myriad of diagnostics, was 1622 sec. Subsequent runs were primarily to determine the accuracy of reducing the numbers of particles emitted and increasing the time step. Since the time step is not Courant limited by the electromagnetic calculation as long as it is below  $2.2 \times 10^{-10}$  sec, a  $10^{-10}$  sec time step was chosen as an optimum from both cost and pulse resolution viewpoints. By reducing the particle emission to 70 per cycle and using the  $10^{-10}$  sec time step, CPU time dropped almost an order of magnitude to 225 sec, with an accuracy of a few percent in quantities characterized by long wavelengths. This was achieved by using nonindependent energy bin selection, that is, by constraining the energy bin choice so that an equal number from each bin is emitted per cycle. Surface currents in the cylinder midplane are shown in Figure 8. The upper curve is from the benchmark run, the lower from the few particle, long time step run. The closeness of these results implies that, at least for the simple geometry considered, accurate SGEMP surface currents can be obtained with very short computations.



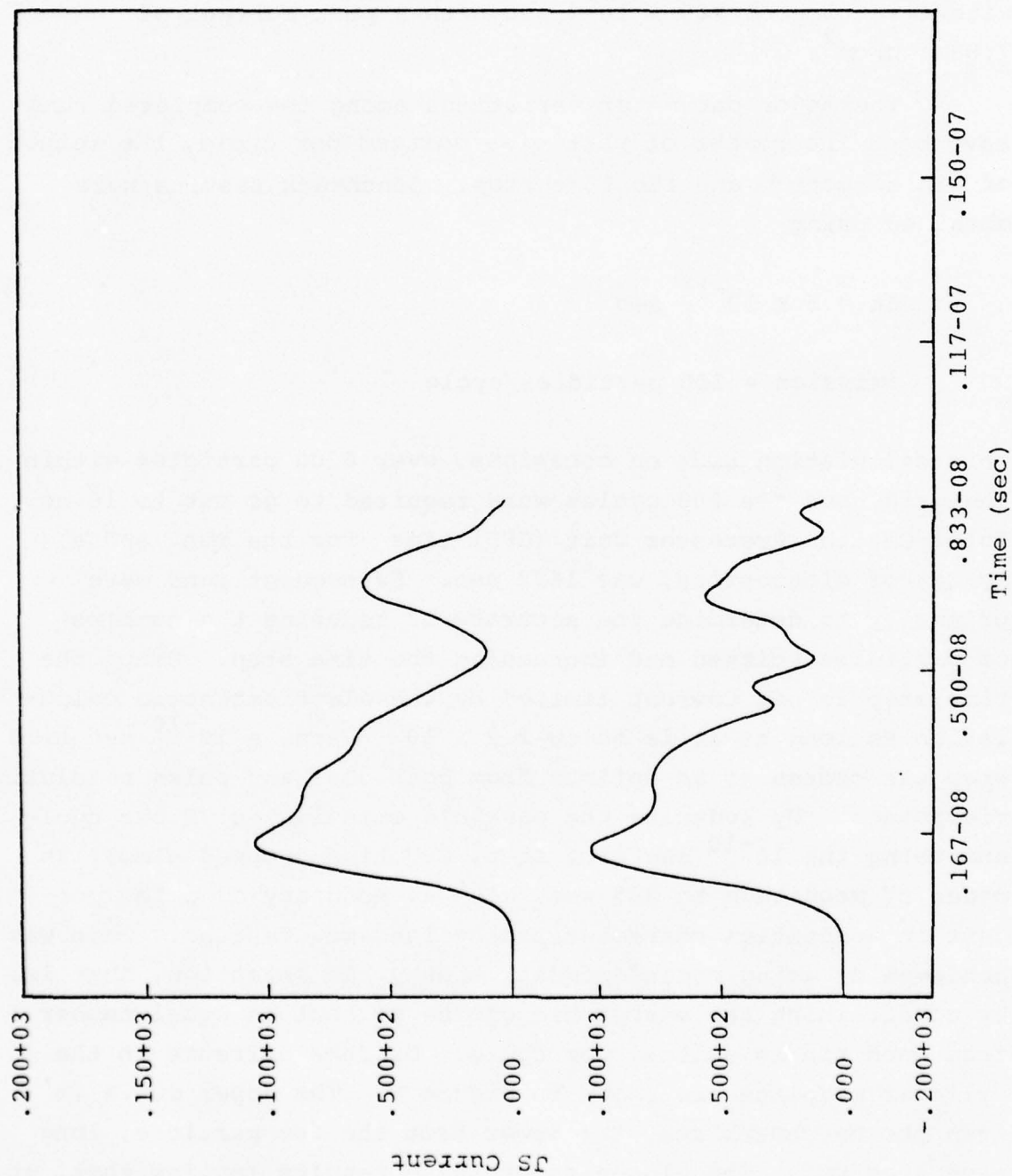


Figure 8 - Midplane surface currents as a function of time. The upper curve is the benchmark calculation; the lower used conditional bin selection and required only 3 minutes of CPU time.

The production runs had

$$\Delta t = 10^{-10} \text{ sec}$$

$$\text{emission} = 140 \text{ particles/cycle}$$

Typical runs used 5 minutes of CPU time and had a maximum of around 1500 particles in the mesh at any one time. The maximum deviation from the desired net emission current was less than 6 percent, while for 70 percent of the cycles, the emission current was within 3 percent of the desired triangular ramp.

The 5 cm radius support rod was inserted by setting the electric field component in the z-direction to zero for the first 10 zones near the axis. For the 1 cm radius support, a set of radial electric fields and  $\phi$  component magnetic fields 1 cm off axis was constructed. Maxwell's equations were solved for these positions using first-order differences. However, the  $[(1/r)(\partial/\partial r)rB_\phi]$  contribution to  $E_z$  near the axis was no longer a centered first-order difference and, as a result, was accurate only to order  $\Delta R$  (as opposed to the rest of the grid where the centered differences were accurate to order  $\Delta R^2$ ).

Skin currents at points C and E (see Figure 1) are shown in Figures 9 and 10. These currents are in amperes per meter and are obtained by multiplying the surface magnetic fields (in gauss) by 79.58. The most prominent feature of the midplane currents (Figure 9) is the second peak occurring approximately 5 nanoseconds after the first peak. One possible mode that would give use to this second peak is that of a wave generated at point B, going out to the wall radially and being reflected back in. The path length of such a wave differs by about 1.5 meters from the direct B to C distance.

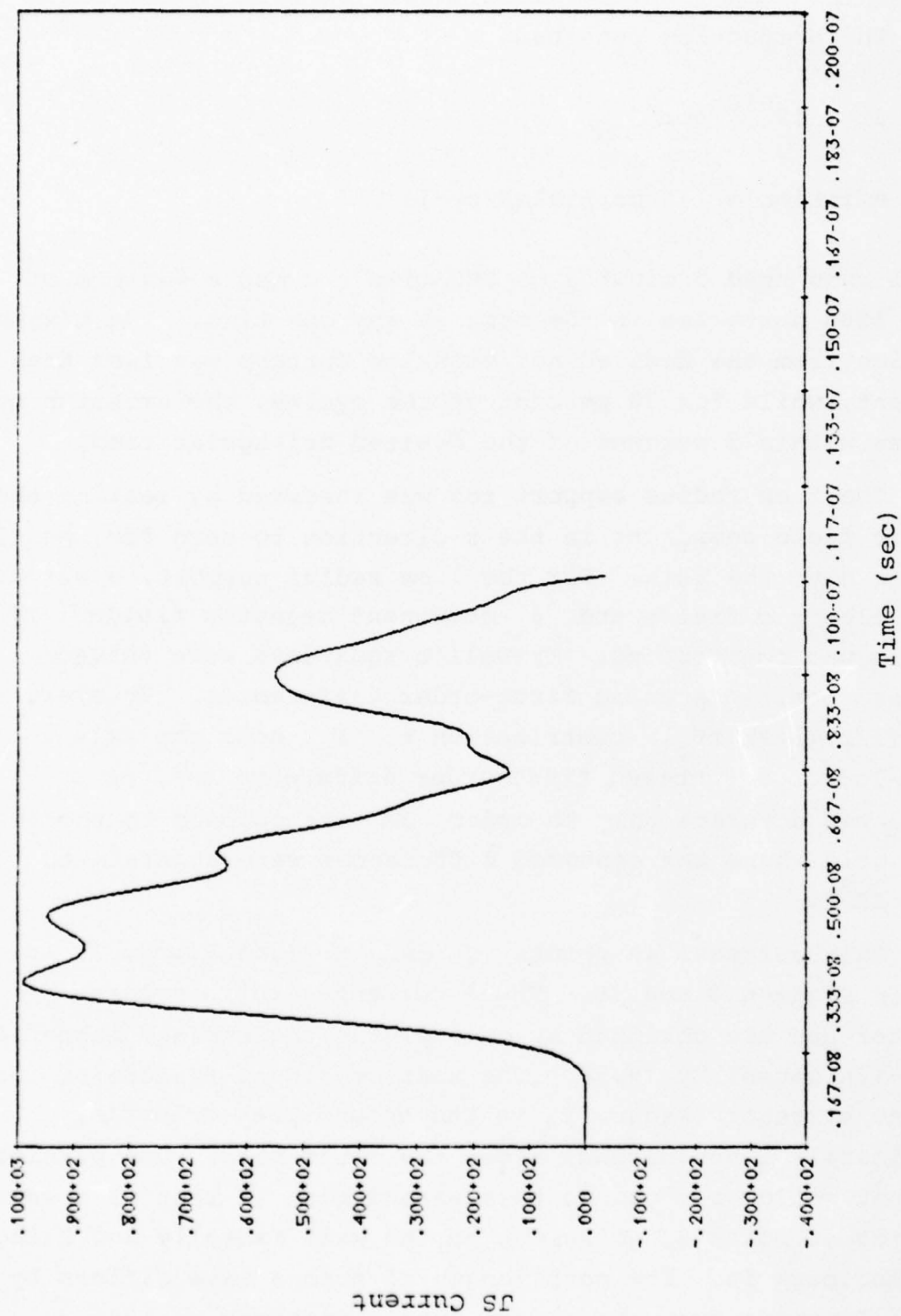


Figure 9 - The surface current at point C in amperes per meter. This current did not vary as a function of support rod diameter.

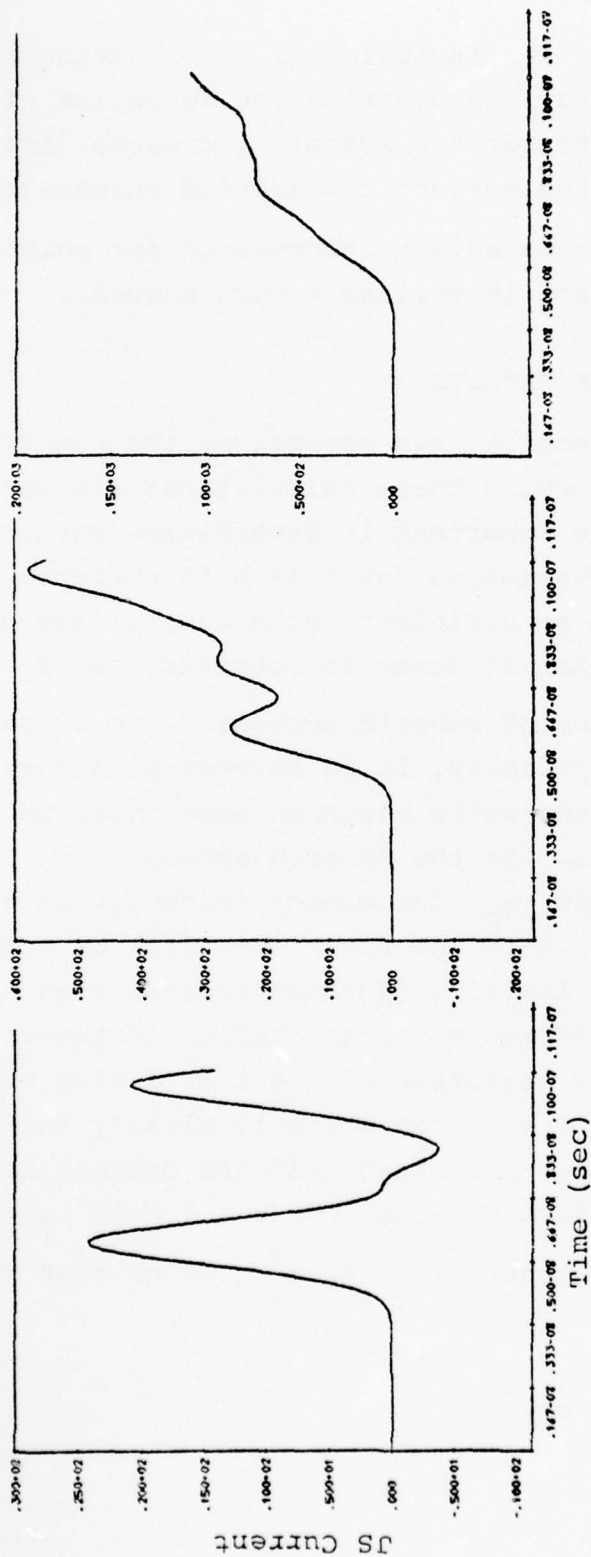


Figure 10 - The surface currents in amperes per meter at point E for the three different rod diameters. From left to right, the plots are for 0-, 2-, 10-cm-diameter supports.



In Figure 10, the inclusion of a conducting support allows charge to escape, preventing the formation of a "sloshing" mode. As the diameter of the support increases, its inductance decreases, so that the current transmitted reaches higher values.

Complete time-dependent information for points A through G has been plotted and is available upon request.

### 2.3 DISCUSSION OF RESULTS

In this subsection, two aspects of the computational techniques used in performing these calculations are examined: (1) Is subgrid screening important in determining particle dynamics and SGEMP response variables (such as skin currents)? (2) Is the hybrid approach an efficient technique, or are ordinary EM codes competitive when it comes to computer costs?

The importance of subgrid screening can be shown in several ways. Analytically, it is an easy procedure to show that if, for a monoenergetic electron beam in an EM code,  $\Delta x \gg v/\omega_p$  where  $\Delta x$  is the EM grid spacing,  $v$  is the emission velocity and  $\omega_p$  the plasma frequency of the beam, the electric field within the first zone will be described incorrectly since the limiting distance is less than a zone size. Since the finite difference representation of Maxwell's equations assumes linear variation of electric fields within a zone, the finite difference representation is clearly inappropriate. For the case in point, more than half the current is composed of electrons below 12 keV in energy ( $v \sim 7 \times 10^9$  cm/sec).

An emitted current of  $1 \text{ A/cm}^2$  (1/7 of peak value) gives a plasma frequency

$$\omega_p \approx 2 \times 10^9 \text{ sec}^{-1}$$

and a limiting distance

$$v/\omega_p \approx 3.5 \text{ cm}$$

Therefore, the majority of the electrons should limit well within the 10 cm zone size for almost the entire duration of the pulse. Consequently, one would expect significant field variations within zones bordering the emitting surface. Figure 11 is a plot of the normal component of the electric field on a particle in the near axis zone as a function of distance from the emitting surface. The departure from linearity is obvious. Figure 12 shows the positions of the particles at 3 nanoseconds into the calculation. The high degree of limiting within 10 centimeters is apparent.

How this nonlinear electric field behavior reflects itself in measurable quantities was examined by running the zero radius support calculation without the subgrid resolution. As is expected, the induced currents are much greater, and are almost a factor of 3 more than calculated with SQUID grid. The dipole field is incorrect near the surface since it exerts too little force on low-energy particles, and as a result, their contribution to the dipole current is unphysically large. We conclude that if large electromagnetic zones are used in this calculation, subgrid electric field corrections must be made.

Even though the SQUID technique enables one to employ large electromagnetic zones, the particle pushing and field calculations are more complicated than conventional EM codes. The relevant question then concerns the cost effectiveness of the hybrid technique. In this area, the results seem quite encouraging.

Based on the spatial resolution required to perform an accurate treatment of the heavily space-charge-limited region near the emitting surface, the SQUID zone chosen was 0.5 cm.

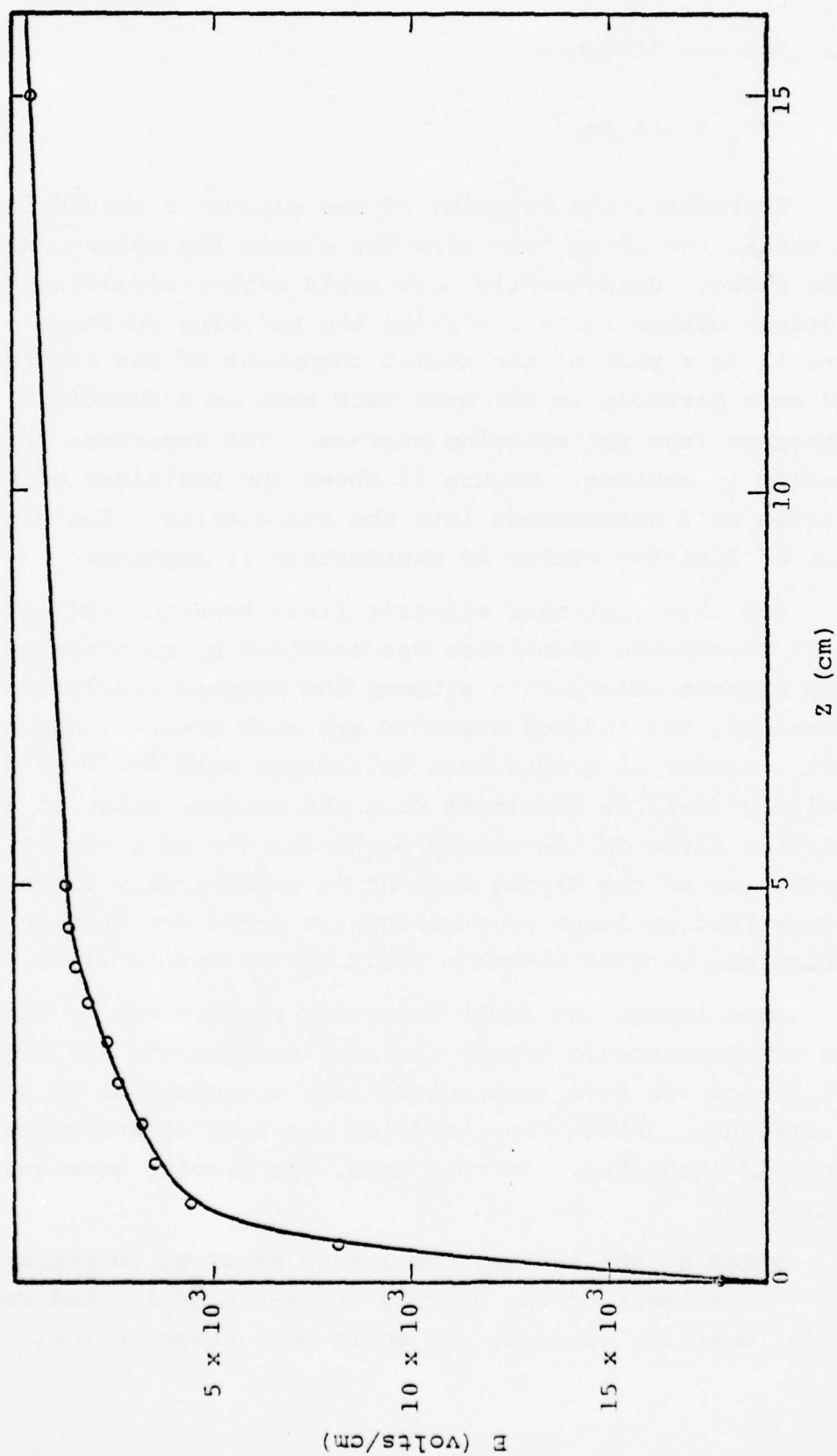


Figure 11 - The perpendicular component of the electric field as a function of distance from the surface 3 nanoseconds into the calculation. An electromagnetic grid zone is 10 cm long. The field strength varies in nonlinear fashion an order of magnitude within the first electromagnetic code zone.

BEST AVAILABLE COPY

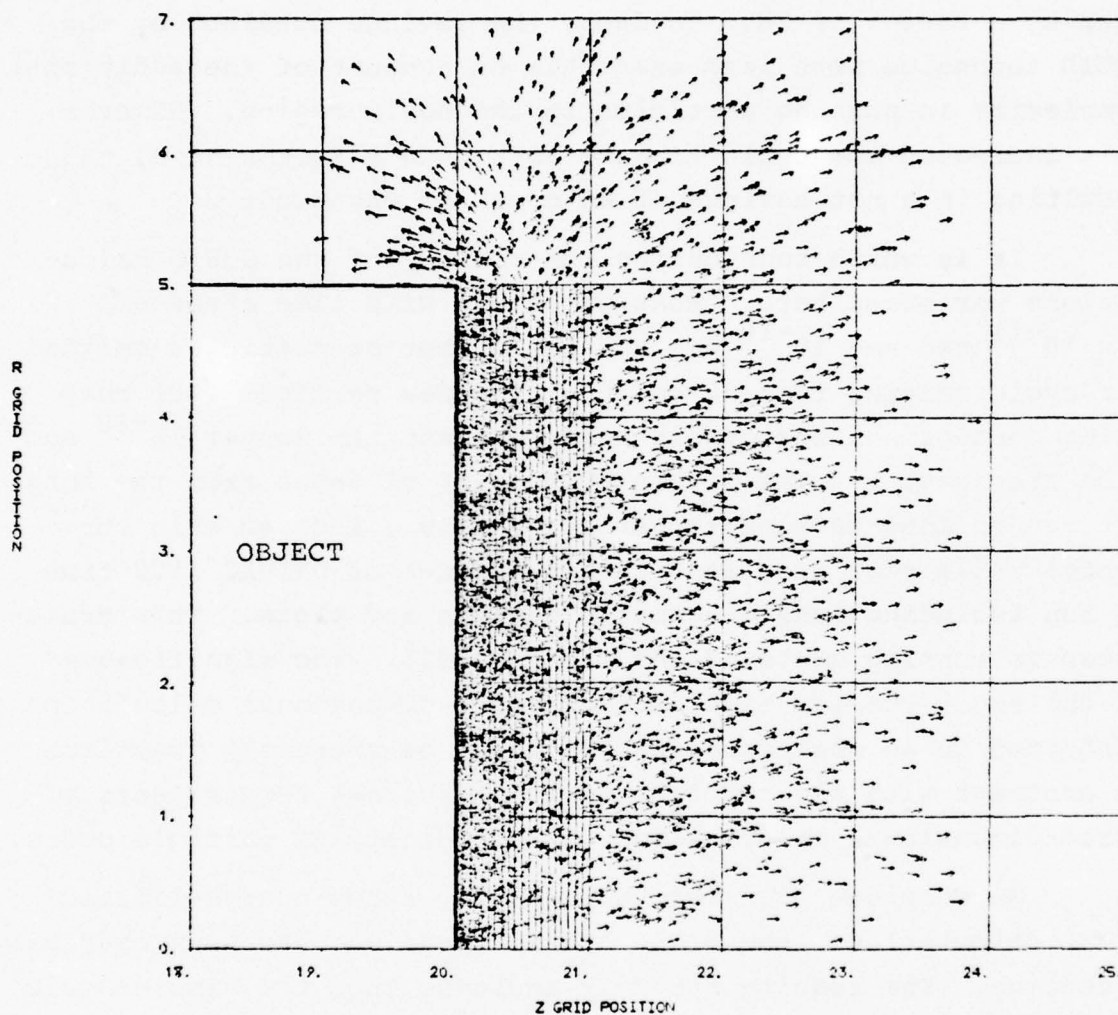


Figure 12 - The electron sheath 3 nanoseconds into the problem. A large grid cell is 10 cm, the SQUID grid spacing is 0.5 cm.



The EM grid spacing was 10 cm. In order to achieve the same resolution by a purely "brute-force" means it would have been necessary to reduce the EM grid spacing and hence the time step by a factor of 20. In fact, the savings obtained by the SQUID technique were less than this on account of the additional complexity in pushing particles in the SQUID region. However, this increased the cycle time by less than a factor of 2, thus resulting in a net savings of an order of magnitude.

It is worth considering the economy of the SQUID calculations performed here. Runs were made with time steps of  $5 \times 10^{-11}$  sec and  $10^{-10}$  sec and the number of particles emitted per cycle ranging from 60 to 300. The few particle (70) runs using conditional energy bin selection and the longer  $10^{-10}$  sec time step gave results within 10 percent of those from the longest run on long-wavelength variables (e.g., induced skin currents) while requiring less than 5 minutes of UNIVAC 1108 time to run including long diagnostic outputs and plots. This translates to running costs of the order of \$15. The significance of the short running time is that three-dimensional calculations performed in an analogous fashion would be extremely practical in contrast with the computer time and storage requirements of three-dimensional calculations using ordinary EM particle codes.

We conclude that for these highly space-charge-limited SGEMP calculations the SQUID hybrid technique has been extremely effective. The results strongly indicate that the dipole-SQUID theory, as discussed in Section 2.1 of this report, contains the physics relevant to SGEMP. While a very fine zoned electromagnetic particle code also contains the relevant physics, it automatically follows unimportant short-wavelength transverse fields. The time step requirements of SQUID are of the order  $\beta$  of the lowest energy electrons times that of an ordinary EM code of comparable spatial resolution. For the examples presented, all of which have 0.5 cm resolution, the conservative  $10^{-10}$  sec

time step is more than a factor of 6 larger than the largest stable time step for an ordinary electromagnetic code. Thus, SQUID enables one to save a large percentage of computer time with no loss in accuracy.

### SECTION III

#### A TECHNIQUE FOR TREATING SMALL CURRENT CARRYING STRUTS IN ELECTROMAGNETIC PARTICLE CODES

The prediction of the electromagnetic response of a satellite to an external impulse, caused for example by a short ( $10^{-8}$  sec) pulse of X rays, presents a formidable computational problem. The state-of-the-art for the self-consistent determination of trajectories of electrons and the electromagnetic field generated by them is well developed for many two-dimensional problems. Where there are highly disparate geometrical length scales, however, as in a hollow right circular cylinder of radius  $R$  with an axially centered strut of radius  $a \ll R$ , either the computational mesh must be extremely fine or other methods for treating small scale lengths must be developed. In this section, methods are formulated for treating thin struts ( $a$  in the above examples) in both two- and three-dimensions. A primary result of the formulation is the retention of a spatial difference mesh that is appropriate for the larger scale length, together with the relatively greater economy in computation associated with the longer timestep that is permitted (by the Courant stability condition) in the staggered-leapfrog finite difference scheme for solving Maxwell's equations.

For the purposes which follow, the Maxwell equations governing the evolution in time of the electric and magnetic fields  $\vec{E}$  and  $\vec{B}$ , respectively, are written in cgs units

$$\nabla \times \vec{E} = - \frac{1}{c} \frac{\partial \vec{B}}{\partial t}$$
$$\nabla \times \vec{B} = \frac{4\pi \vec{j}}{c} + \frac{1}{c} \frac{\partial \vec{E}}{\partial t}$$

where  $\vec{j}$  is the current density and  $c$  the velocity of light.

### 3.1 FIELDS NEAR A STRUT

First consider the fields in the vicinity of a perfectly conducting strut of radius  $a$ . In a cylindrical coordinate system whose  $z$ -axis coincides with the strut axis,

$$\frac{\partial E_{\rho}}{\partial z} - \frac{\partial E_z}{\partial \rho} = -\frac{1}{c} \frac{\partial B_{\theta}}{\partial t} \quad (1)$$

Near the strut,

$$B_{\theta}(\rho, z, t) = \frac{a B_{\theta}(a, z, t)}{\rho} \quad (2)$$

$$E_{\rho}(\rho, z, t) = \frac{a E_{\rho}(a, z, t)}{\rho} \quad (3)$$

$$2\pi a B_{\theta}(a, z, t) = \frac{4\pi I(z, t)}{c} \quad (4)$$

and

$$2\pi a E_{\rho}(a, z, t) = 4\pi Q(z, t) \quad (5)$$

The current  $I$  carried by the strut and its charge  $Q$  per unit length are related by the continuity equation

$$\frac{\partial Q}{\partial t} + \frac{\partial I}{\partial z} = 0 \quad (6)$$

Here, we have assumed that the strut neither emits nor absorbs charge.

Integrating Equation (1) from  $a$  to  $\rho$  gives

$$E_z(\rho) = \frac{\partial}{\partial z} \int_a^{\rho} E_{\rho}(\rho') d\rho' + \frac{1}{c} \frac{\partial}{\partial t} \int_a^{\rho} B_{\theta}(\rho') d\rho' \quad (7)$$



since  $E_z(a) = 0$ . From Equations (2) through (5)

$$E_z(\rho) = 2 \ln(\rho/a) \frac{\partial Q}{\partial z} + \frac{2}{c^2} \ln(\rho/a) \frac{\partial I}{\partial t} \quad (8)$$

The area average of  $E_z$  over a cell is given by

$$E_{z,av} = C^{-1} \frac{\partial Q}{\partial z} + L \frac{\partial I}{\partial t} \quad (9)$$

where

$$C^{-1} = 2 \langle \ln(\rho/a) \rangle \quad (10)$$

and

$$L = \frac{1}{c^2} C^{-1} \quad (11)$$

are the capacitance and inductance, respectively, per unit length of the strut. Here,  $\langle f \rangle$  denotes an area average of  $f$  over a cross section of the cell normal to the strut. If the cross section of area  $A$  is approximated by a cylindrical cell of radius  $R = \sqrt{\frac{A}{\pi}}$  centered on the strut axis, then

$$C^{-1} = \frac{4\pi}{A} \int_a^R \rho \ln(\rho/a) d\rho \quad (12)$$

$$= 2 \ln(R/a) + a^2/R^2 - 1 \quad (13)$$

In obtaining Equation (9), it has been assumed that the dominant local fields are quasi-static and, moreover, are axisymmetric in the coordinate system centered on the strut. These assumptions exclude very short wavelength modes corresponding, for example, to variations depending on the azimuthal angle. Such short wavelength excitations are probably not very important in any practically occurring SGEMP context.

### 3.2 3-D DIFFERENCE EQUATIONS

For three-dimensional (3-D) calculations, we adopt Cartesian geometry and a computational grid whose cells are identical and whose three mutually perpendicular edges have arbitrary lengths. The centering scheme is depicted in Figure 13. Letting  $(i,j,k)$  be the coordinates of a cell center in units of the lengths of the basic cell edges, we center the field and current components according to the following scheme:

$$j_x, E_x: (i+\frac{1}{2}, j, k+\frac{1}{2})$$

$$j_y, E_y: (i, j+\frac{1}{2}, k+\frac{1}{2})$$

$$j_z, E_z: (i, j, k)$$

$$B_x: (i, j+\frac{1}{2}, k)$$

$$B_y: (i+\frac{1}{2}, j, k)$$

$$B_z: (i+\frac{1}{2}, j+\frac{1}{2}, k+\frac{1}{2})$$

Using a staggered-leapfrog scheme in which  $\vec{E}$  and  $\vec{B}$  are advanced in a fully space-and-time centered manner, the difference forms of Maxwell's equations become

$$\vec{B}^{t+\frac{1}{2}}(i, j, k) - \vec{B}^{t-\frac{1}{2}}(i, j, k) = -c\Delta t (\nabla_D \times \vec{E})^t(i, j, k) \quad (14)$$

$$\begin{aligned} \vec{E}^{t+1}(i, j, k) - \vec{E}^t(i, j, k) &= c\Delta t (\nabla_D \times \vec{B})^{t+\frac{1}{2}}(i, j, k) \\ &\quad - \frac{4\pi}{c} \vec{j}^{t+\frac{1}{2}}(i, j, k) \end{aligned} \quad (15)$$

The subscript  $D$  denotes the difference gradient,

$$\begin{aligned} (\nabla_D \times \vec{A})_x(i, j, k) &= \frac{A_z(i, j+\frac{1}{2}, k) - A_z(i, j-\frac{1}{2}, k)}{\Delta y} \\ &\quad - \frac{A_y(i, j, k+\frac{1}{2}) - A_y(i, j, k-\frac{1}{2})}{\Delta z} \end{aligned} \quad (16)$$

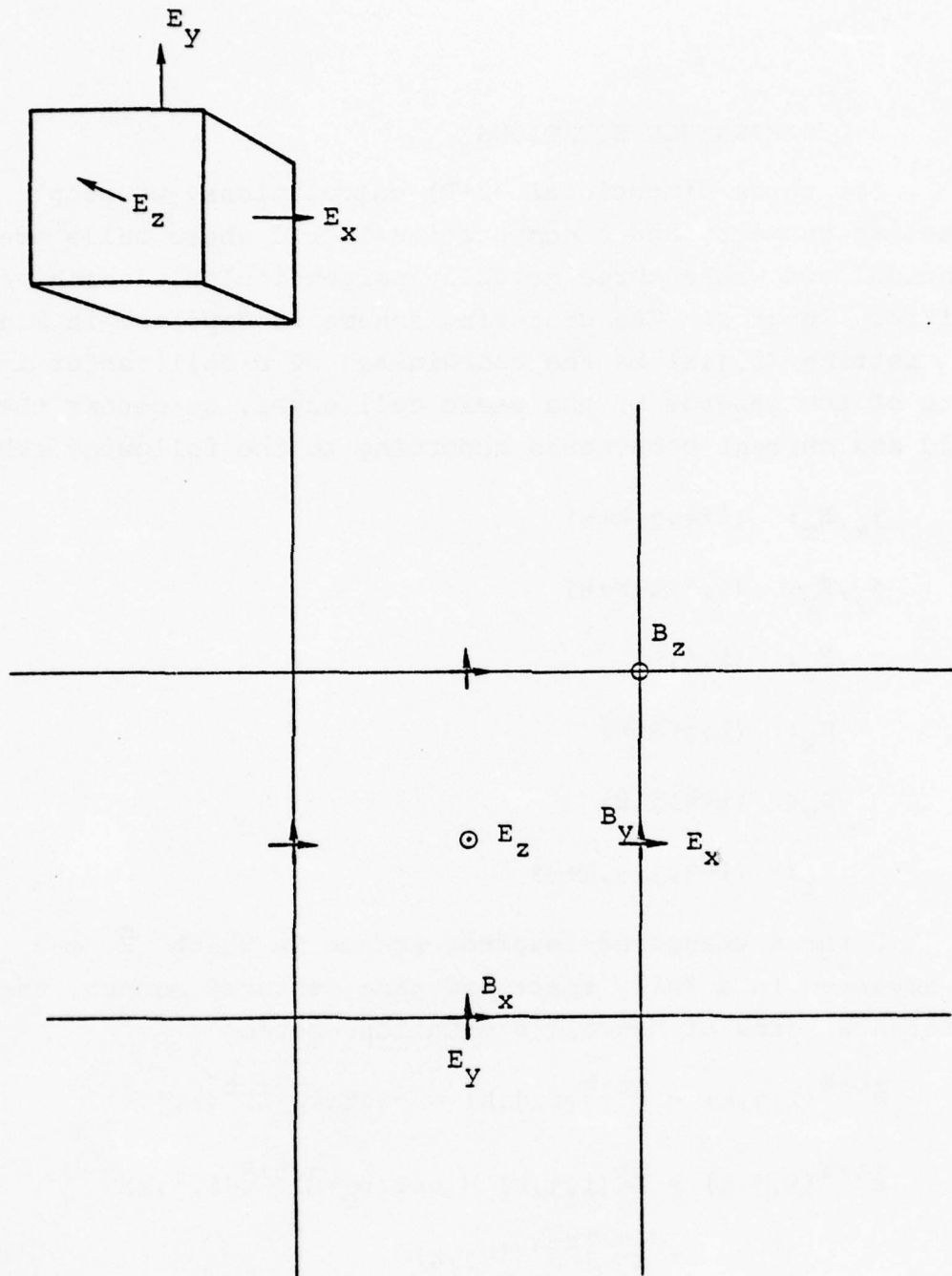


Figure 13 - 3-D strut calculation.

$$(\nabla_D \times \vec{A})_y(i, j, k) = \frac{A_x(i, j, k+\frac{1}{2}) - A_x(i, j, k-\frac{1}{2})}{\Delta z} - \frac{A_z(i+\frac{1}{2}, j, k) - A_z(i-\frac{1}{2}, j, k)}{\Delta x} \quad (17)$$

$$(\nabla_D \times \vec{A})_z(i, j, k) = \frac{A_x(i, j+\frac{1}{2}, k) - A_x(i, j-\frac{1}{2}, k)}{\Delta y} - \frac{A_y(i+\frac{1}{2}, j, k) - A_y(i-\frac{1}{2}, j, k)}{\Delta x} \quad (18)$$

and  $i, j, k$  are integral or half-odd integral according to the centering scheme of Figure 13.

The foregoing equations are intended to apply for systems where there is no great disparity in length scales. For systems with highly dissimilar length scales, such as the cylinder with struts, the foregoing equations must be modified to avoid the fine-zoning associated with a small strut radius.



### 3.3 LINEAR STRUT IN A 3-D GEOMETRY

Consider a linear strut whose axis, parallel to the z-direction, pierces the x-y plane at the position (I,J) where  $E_z$  is centered. The grid is sufficient to resolve spatial variations of the electromagnetic field except within the zones through which the strut passes. There, the local fields vary according to Equations (3) and (4). Thus, the difference Equations (14) and (15) apply at all space points and for all field components with the following exceptions:

a) the equations for  $B_x^{t+\frac{1}{2}}(I, J+\frac{1}{2}, k) - B_x^{t-\frac{1}{2}}(I, J+\frac{1}{2}, k)$

and  $B_y^{t+\frac{1}{2}}(I+\frac{1}{2}, J, k) - B_y^{t-\frac{1}{2}}(I+\frac{1}{2}, J, k)$

and

b) the equations for  $E_z^{t+1}(I, J, k) - E_z^t(I, J, k)$ .

The required modifications of the equations for advancing the magnetic field components  $B_x$  and  $B_y$  are obtained by setting  $E_z(I, J, k) = E_{z,av}$  in Equation (14). Thus, for example,

$$B_x^{t+\frac{1}{2}}(I, J+\frac{1}{2}, k) - B_x^{t-\frac{1}{2}}(I, J+\frac{1}{2}, k) = -c\Delta t \left[ \frac{E_z^t(I, J+1, k) - E_{z,av}^t(I, J, k)}{\Delta y} - \frac{E_y^t(I, J+\frac{1}{2}, k+\frac{1}{2}) - E_y^t(I, J+\frac{1}{2}, k-\frac{1}{2})}{\Delta z} \right] \quad (19)$$

Now it remains only to alter the equations for advancing  $E_z(I, J, k)$  in time. The required modifications are based upon Equations (6) and (9) together with Equation (20),

$$\frac{1}{c} \frac{E_{z,av}^{t+1}(I,J,k) - E_{z,av}^t(I,J,k)}{\Delta t} = - \frac{4\pi}{c} j_z^{t+\frac{1}{2}}(I,J,k) - \frac{4\pi}{c} I^{t+\alpha}(k) + (\nabla \times \vec{B})_z^{t+\frac{1}{2}}(I,J,k) \quad (20)$$

where  $E_{z,av}$  is, again, the area average of  $E_z$  over a cross section of the zone normal to the strut.

$$I^{t+\alpha} = \alpha I^{t+1} + (1-\alpha) I^t$$

is the current carried by the strut, and the parameter  $\alpha$  indicates the degree of implicitness. For  $\alpha = 1(0)$ , the current is treated in a fully implicit (explicit) manner; for  $\alpha = \frac{1}{2}$ , the current is time centered and the treatment of the strut current is half-implicit. The two additional Equations, (6) and (9), are sufficient to describe the system which now contains the two additional variables  $I(z)$  and  $Q(z)$ .

For advancing  $I$  and  $Q$ , Equations (6) and (9) are written in the fully space and time centered form

$$L \frac{I^{t+1}(k) - I^t(k)}{\Delta t} = -C^{-1} \left[ \frac{Q^{t+\frac{1}{2}}(k+\frac{1}{2}) - Q^{t+\frac{1}{2}}(k-\frac{1}{2})}{\Delta z} \right] + \frac{1}{2} \left[ E_{z,av}^{t+1}(k) + E_{z,av}^t(k) \right] \quad (21)$$

$$\frac{Q^{t+\frac{1}{2}}(k+\frac{1}{2}) - Q^{t-\frac{1}{2}}(k+\frac{1}{2})}{\Delta t} = - \frac{I^t(k+1) - I^t(k)}{\Delta z} \quad (22)$$

Here, the dependence on all discretized spatial variables except those indicating position along the strut has been suppressed.

The stability of the computational scheme corresponding to Equations (20) through (22) with  $\alpha = 1$  and  $\alpha = \frac{1}{2}$  has been demonstrated in the two-dimensional calculations described in Section 6. In the context of stability, it is worth noting

that Equations (20) through (22) depart from the explicit staggered-leapfrog scheme that is commonly employed in the solution of Maxwell's equations. If the conventional scheme were retained throughout, then  $I$  and  $Q$  would be centered at  $t + \frac{1}{2}$  and  $t$ , respectively. Equation (20) would have  $\alpha = \frac{1}{2}$  and Equations (21) and (22) could be replaced by the explicit forms

$$L \frac{I^{t+\frac{1}{2}}(k) - I^{t-\frac{1}{2}}(k)}{\Delta t} = -C^{-1} \left[ \frac{Q^t(k+\frac{1}{2}) - Q^t(k-\frac{1}{2})}{\Delta z} \right] + E_{z,av}^t(k) \quad (23)$$

$$\frac{Q^{t+1}(k+\frac{1}{2}) - Q^t(k+\frac{1}{2})}{\Delta t} = - \frac{I^{t+\frac{1}{2}}(k+1) - I^{t+\frac{1}{2}}(k)}{\Delta z} \quad (24)$$

For sufficiently small values of  $L$ , i.e., for rods of radius comparable with the cell size, we conjecture that, in contrast to Equations (21) and (22), the stability of these equations require a time increment more restrictive than that imposed by the Courant conditions over the portion of the mesh through which struts do not pass; viz,

$$\Delta t \leq \frac{\Delta z}{c}$$

### 3.4 TWO-DIMENSIONAL SIMULATIONS OF STRUT GEOMETRY

Since off-axis struts in an otherwise axisymmetric geometry pose an inherently three-dimensional problem, the development in the previous section was three-dimensional from the outset. On the other hand, in a cylinder with identical struts parallel to the z-axis located at the same radial distance from the cylinder axis, and equally spaced in angle, the azimuthally averaged fields for the mode of highest angular symmetry satisfy precisely the two-dimensional field equations of axisymmetric cylindrical  $r, z$  geometry. The mode of highest angular symmetry is the only one excited, for example, by a radially uniform pulse of X rays incident normally on one end of the cylinder.

Particular interest is attached to the first two of the relevant Maxwell equations given below in the vicinity of the radial location of the struts:

$$-\frac{1}{c} \frac{\partial B_{\theta}}{\partial t} = \frac{\partial E_r}{\partial z} - \frac{\partial E_z}{\partial r} \quad (25)$$

$$\frac{1}{c} \frac{\partial E_z}{\partial t} + \frac{4\pi}{c} j_z = \frac{1}{r} \frac{\partial}{\partial r} (r B_{\theta}) \quad (26)$$

$$\frac{1}{c} \frac{\partial E_r}{\partial t} + \frac{4\pi}{c} j_r = - \frac{\partial B_{\theta}}{\partial z} \quad (27)$$

Here, the indicated fields are azimuthally averaged and  $r$  is measured from the axis of the cylinder (not from a strut axis).

The difference equations in the strut-bearing zones, which have radial index,  $I$ , are



$$\begin{aligned}
& - \frac{1}{c} \left[ \frac{B^{t+\frac{1}{2}}(I \pm \frac{1}{2}, j + \frac{1}{2}) - B^{t-\frac{1}{2}}(I \pm \frac{1}{2}, j + \frac{1}{2})}{\Delta t} \right] \\
& = \frac{E_r^t(I \pm \frac{1}{2}, j+1) - E_r^t(I \pm \frac{1}{2}, j)}{\Delta z} - \frac{E_z^t(I \pm \frac{1}{2} + \frac{1}{2}, j + \frac{1}{2}) - E_z^t(I \pm \frac{1}{2} - \frac{1}{2}, j + \frac{1}{2})}{\Delta r}
\end{aligned} \tag{28}$$

$$\begin{aligned}
& \frac{1}{c} \frac{E_z^{t+1}(I, j) - E_z^t(I, j)}{\Delta t} + \frac{4\pi}{c} \frac{I(j)}{2\pi r_I \Delta r} + \frac{4\pi}{c} j_z(I, j) \\
& = \frac{1}{r_I} \frac{(r_I + \frac{\Delta r}{2}) B^{t+\frac{1}{2}}(I + \frac{1}{2}, j) - (r_I - \frac{\Delta r}{2}) B^{t+\frac{1}{2}}(I - \frac{1}{2}, j)}{\Delta r}
\end{aligned} \tag{29}$$

The quantity  $I(j)$  is the total current in all of the struts at the  $z$  location with index  $j$ .

To complete the description requires a determination of the current  $I$ ; the required relations will be given in the form of Equations (6) and (9). Equation (6) is simply the equation of continuity along the strut. Equation (9) must be derived from a heretofore unused Maxwell equation which describes departures from azimuthal symmetry. The presence of current and charge on the struts lead, in fact, to a radial magnetic field,  $B_r$ , which in the highest symmetry case considered here, vanishes on averaging over azimuth. The defining equation

$$- \frac{1}{c} \frac{\partial B_r}{\partial t} = \frac{1}{r} \frac{\partial E_z}{\partial \theta} - \frac{\partial E_\theta}{\partial z}$$

when integrated twice over  $\theta$  along the curve  $r = \text{constant}$  on which the strut axes lie, yields

$$\frac{\pi}{N} E_{z,av} = \frac{r}{c} \frac{\partial}{\partial t} \int_0^{\pi/N} d\theta \int_0^\theta B_r(\theta') d\theta' + r \frac{\partial}{\partial z} \int_0^{\pi/N} d\theta \int_0^\theta E_\theta(\theta') d\theta'$$

where  $N$  is the number of struts and  $\theta_0$  the angle subtended at  $r = 0$  by a strut radius.

For struts separated by a distance  $b \ll r$ , it is reasonable to approximate  $B_r$  and  $E_\theta$  in the manner described in Section 3.1, in which case  $B_r$  and  $E_\theta$  are proportional to the current and charge per unit length, respectively, on the struts. This is a basically quasi-static approximation and requires, as well, that the wavelengths of the fields being computed are also large compared to the strut separation. In practice, this is not always the case, but the considered approximations are about as well as we can do in the two-dimensional simulation of an inherently three-dimensional problem. Results based on these two-dimensional approximations are presented in Section 3.5.

### 3.5 TEST CALCULATIONS

In order to test the difference formulations derived in the previous sections, a series of axially symmetric 2-D electromagnetic calculations was performed. They fall into two general classes. The first consisted of tests of "loaded" struts, that is, small diameter struts connecting large objects so that the dominant features of the system are the strut inductance and the objects' capacitance. The second tests involved the behavior of an isolated radiating rod. Here, the system is inherently electromagnetic in nature with the observable features being the frequency of the radiation and the radiation "resistance" damping oscillations on the rod.

For the "loaded" strut tests, a series of runs was made of a conducting cylinder supported by off-axis cylindrically symmetric struts in a conducting tank. The configuration is shown in Figure 14.

The dimensions of the system are the following:

Inner cylinder: radius 83.5 cm  
length 100 cm  
Outer cylinder: radius 2.5 m  
length 6 m  
Support struts: length 2.6 m  
distance off-axis 41.75 cm

The calculations were performed using FRED/EM-PRECHARGE, a 2-D fully electromagnetic code which has the capability of initializing the fields to satisfy Laplace's equation. The calculational mesh was  $15 \times 30$  with  $\Delta R = 16.7$  cm and  $\Delta Z = 20$  cm, and the timestep chosen was  $3.85 \times 10^{-10}$  second, which is 0.9 of the Courant timestep. Initially, the object was charged to 10 kV with respect to the tank using the PRECHARGE routine, an SOR Laplace solver that generates electric fields which are curl free to machine accuracy. The dominant capacitance of this configuration is just

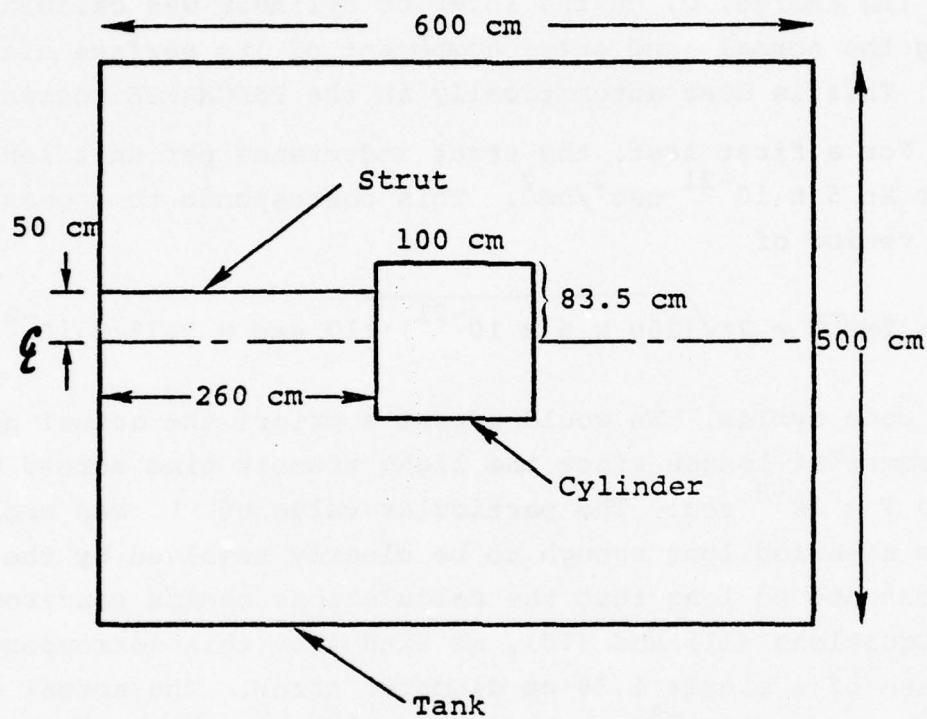


Figure 14 - The configuration used for testing the response of loaded struts.



$$C = \frac{q}{V} = \frac{1.31 \times 10^{-6} \text{ Coulomb}}{10^4 \text{ volts}} = 1.3 \times 10^{-10} \text{ farads}$$

This corresponds to a capacitance of 117 cm (esu).

The charge,  $q$ , on the interior cylinder was calculated by summing the normal (and only) component of its surface electric field. This is done automatically in the PRECHARGE routine.

For a first test, the strut inductance per unit length was set at  $5 \times 10^{-21} \text{ sec}^2/\text{cm}^2$ . This corresponds to a quasi-static period of

$$2\pi\omega^{-1} = 2\pi\sqrt{LC} = 2\pi\sqrt{(260 \times 5 \times 10^{-21}) \cdot 117 \text{ sec}} = 7.75 \times 10^{-8} \text{ sec}$$

or 201 code cycles. We would expect a priori the actual period to be somewhat longer since the light transit time across the tank is  $2 \times 10^{-8} \text{ sec}$ . The particular value of  $L$  was chosen to give a period long enough to be clearly resolved by the code, but not so long that the calculations became ponderous. Using Equations (11) and (13), we find that this corresponds to a case of a single 2.38 cm diameter strut. The actual code period was  $9.34 \times 10^{-8} \text{ sec}$  or  $1.6 \times 10^{-8} \text{ sec}$  longer than the quasi-static prediction. This is quite plausible considering that the period required for information to pass back and forth through the tank is  $4 \times 10^{-8} \text{ second}$ . The current midway along the strut, as a function of time, is shown in Figure 15. The initial conditions excited several modes, accounting for the nonsinusoidal behavior. That the electric field obtained from Equation (20) is indeed appropriate comes from examining the magnetic field a half zone outside the strut at a radius of 50.1 cm. For example, at  $6.11 \times 10^{-8} \text{ sec}$ , the current in the strut 80 cm from the tank wall was 69.6 amperes. Cylindrically averaged, this would generate an average static magnetic field of 0.2777 gauss at 50.1 cm. The code shows a field of 0.2786 gauss, extremely close to the static value. Since only the

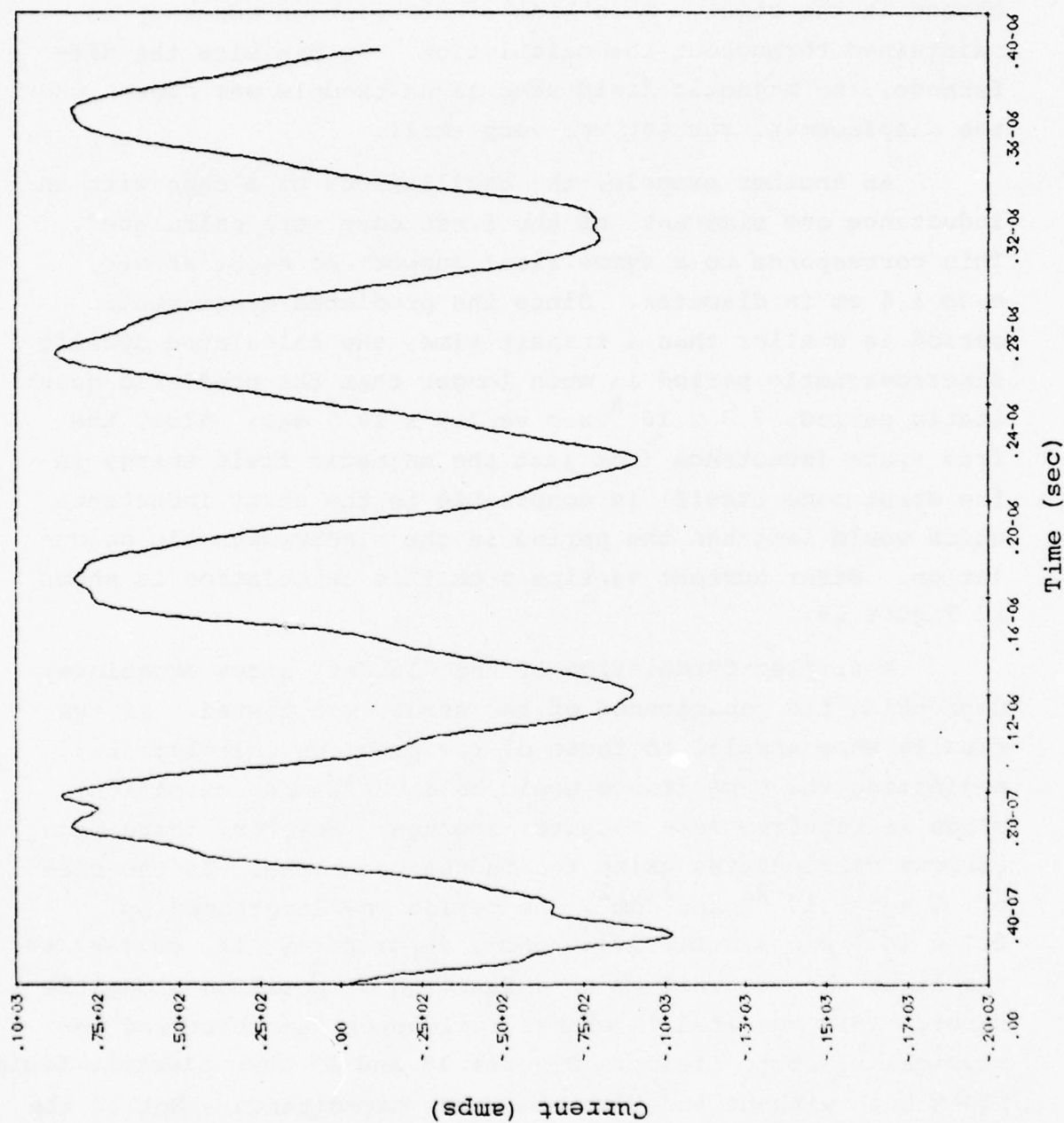


Figure 15 - Strut current vs. time for an induction per unit length of  $5 \times 10^{-2}$  sec<sup>2</sup>/cm<sup>2</sup>.

free space Faraday's equation is used to generate the magnetic field, it shows clearly the correctness of the electric field chosen at the strut. This kind of correlation accuracy is maintained throughout the calculation. To minimize the difference, the magnetic field used as an example was chosen when the displacement current was very small.

As another example, the oscillations of a case with an inductance one sixteenth of the first case were calculated. This corresponds to a symmetrical support of eight struts, each 1.6 cm in diameter. Since the predicted quasi-static period is smaller than a transit time, the calculated dynamic electromagnetic period is much longer than the predicted quasi-static period,  $7.3 \times 10^{-8}$  sec vs.  $1.9 \times 10^{-8}$  sec. Also, the free space inductance (not just the magnetic field energy in the strut zone itself) is comparable to the strut inductance which would lengthen the period in the electromagnetic calculation. Strut current vs. time from this calculation is shown in Figure 16.

A simpler formulation of the "loaded" strut equations, neglecting the capacitance of the strut, was tested. If the results were similar to those of the previous calculations, neglecting the capacitance would be a useful approximation since it requires less computer storage. However, there were serious difficulties using the inductance alone. In the case of  $L = 5 \times 10^{-21}$  sec<sup>2</sup>/cm<sup>2</sup>, the period was lengthened by  $0.7 \times 10^{-8}$  sec (Figure 17). More importantly, the current on the strut was not uniform as a function of position along the strut. This resulted in charge buildup on the strut and unphysical electric fields. Figures 18 and 19 show electric field plots both without and with the strut capacitance. Notice the large fields near the strut in the no capacitance case (Figure 18) and the very small fields near the strut in the capacitance case. The plots were selected in both cases to maximize

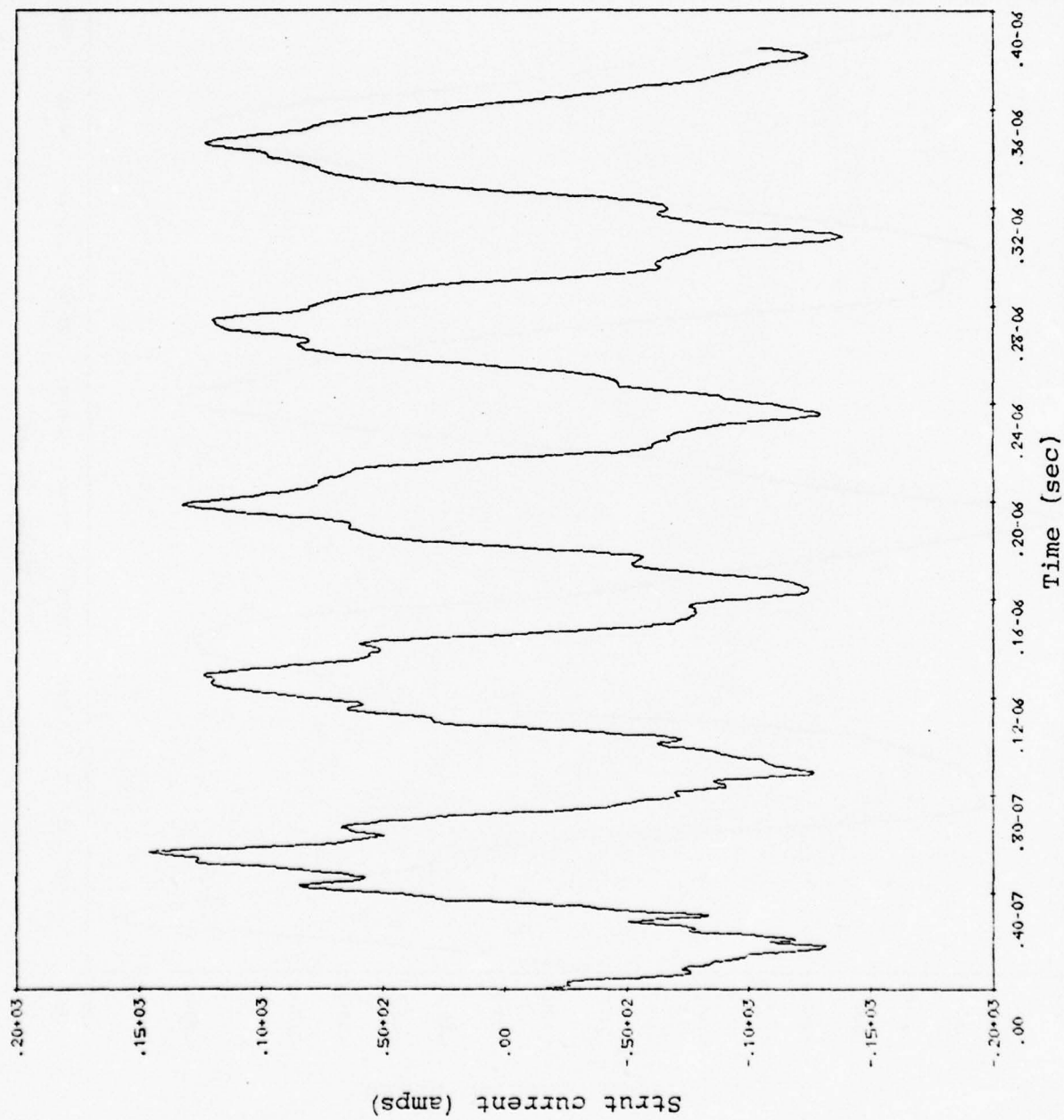


Figure 16 - Strut current vs. time for an inductance per unit length of  $3.125 \times 10^{-22} \text{ sec}^2/\text{cm}^2$ .



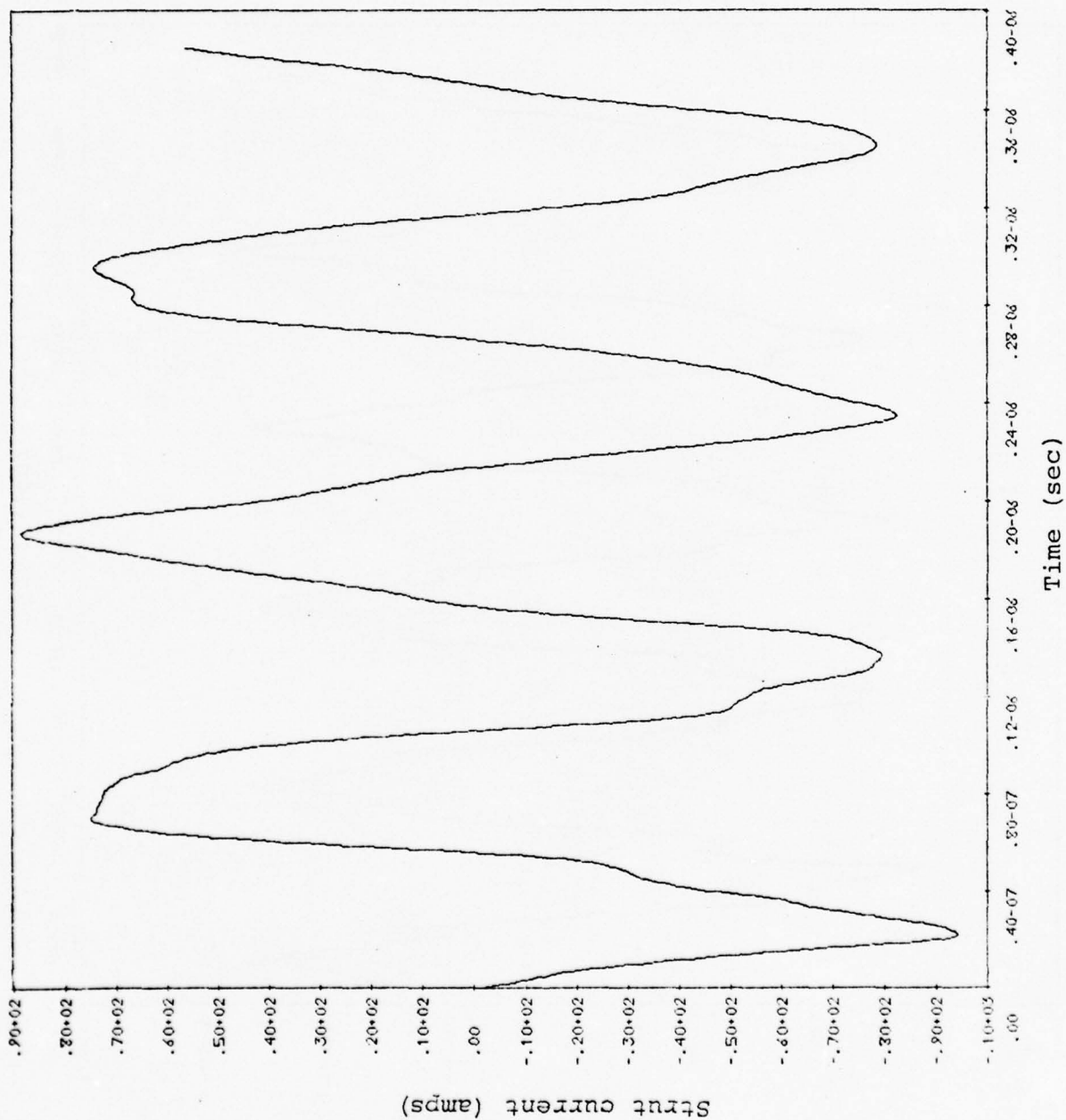


Figure 17 - Strut current vs. time for an inductance per unit length of  $5 \times 10^{-21} \text{ sec}^2/\text{cm}^2$  and no strut capacitance.

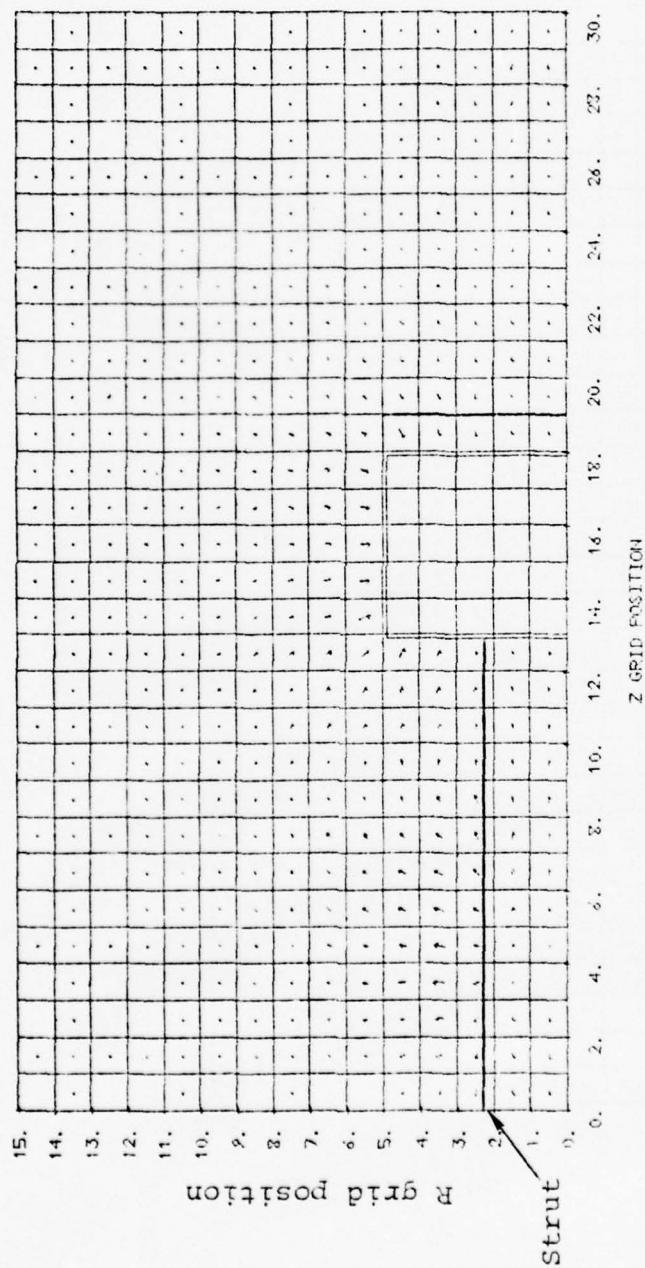


Figure 18 - Electric fields in the example without capacitance.  
Notice large fields along the strut.

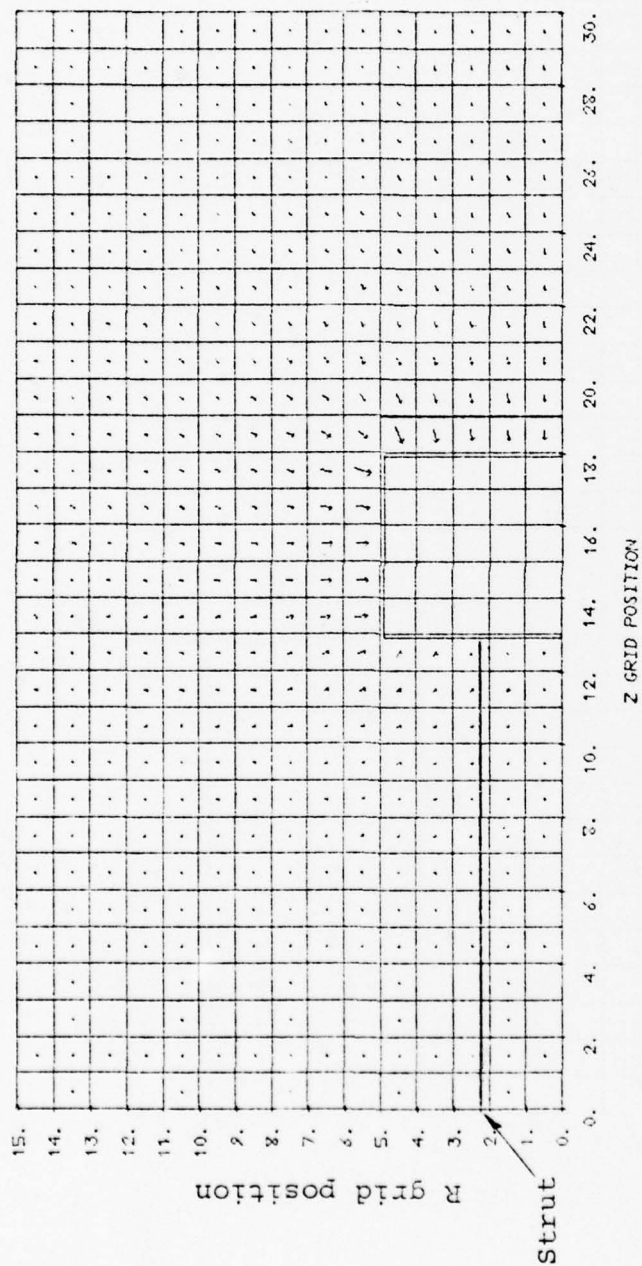


Figure 19 - Electric fields in the case with capacitance.

fields near the struts. The absence of the capacitance prevents current from flowing with a uniform velocity down the strut.

The radiative properties of an isolated strut in a tank were also tested using the FRED/EM code. The first configuration is shown in Figure 20. The discretized strut included six charges and five currents. The zone sizes were as before. Initially, the charge was distributed sinusoidally on the strut. Current vs. time at the strut midpoint is shown in Figure 21. The period is approximately  $8 \times 10^{-9}$  sec, corresponding to a rod length of 120 cm. Figure 22 shows the same configuration with the radial zone size increased to 30 cm. This increases the distance to the radial wall resulting in a "clear" time of  $3 \times 10^{-8}$  sec as compared to  $1.7 \times 10^{-8}$  sec in the case of Figure 21. Figure 23 shows a configuration with the larger  $\Delta R$  and a rod increased in length by two cells (40 cm). The period is now  $10.8 \times 10^{-9}$  sec, corresponding to a strut length of 162 cm. These times have an uncertainty of order 1/2 of time-step (which was  $3 \times 10^{-10}$  sec). This translates to 4.5 cm uncertainties in the strut length. Thus, within the uncertainties, the first two cases radiated like a 120 cm (6 zone) strut, and the second like a 160 cm (8 zone) strut. The nonsinusoidal behavior is due to the initial conditions exciting more than the lowest mode.

One feature worth noting in these isolated strut calculations is the decay in amplitude of the strut current up until the reflected signal returns. This is completely expected due to the power lost from radiation. For the 2.38 cm diameter, 120 cm strut, theory predicts a damping time of  $1.3 \times 10^{-8}$  second. Estimates of the actual numerical damping rate based on Figure 22 agree well with the theory. However, more definitive calculations are required to accurately determine the numerical damping period.



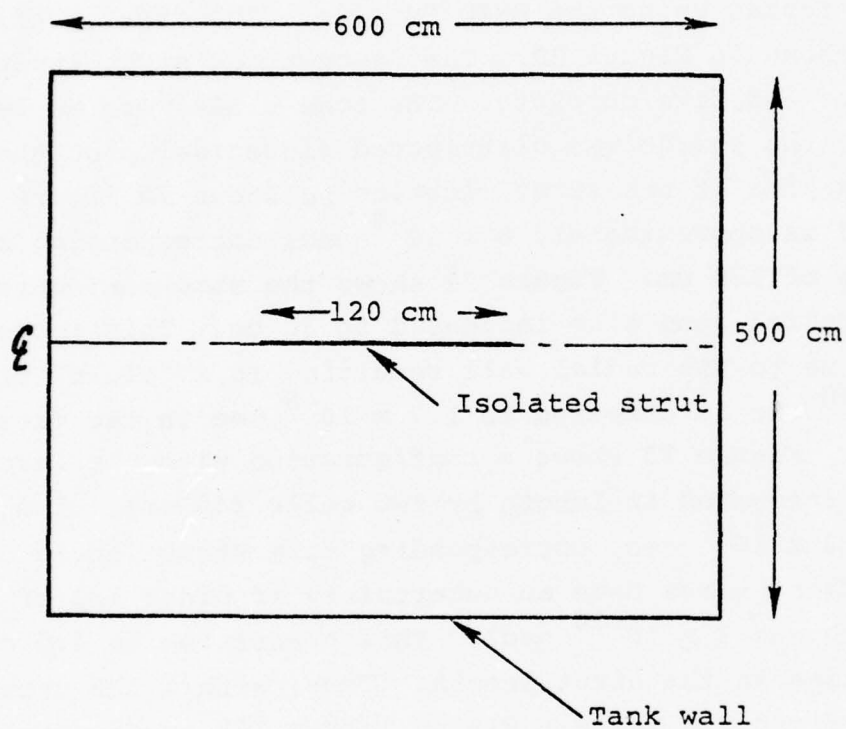


Figure 20 - The configuration used for testing the response of isolated struts. In the second and third cases, the tank diameter was increased from 500 cm to 900 cm in order to lengthen the "clear" time.

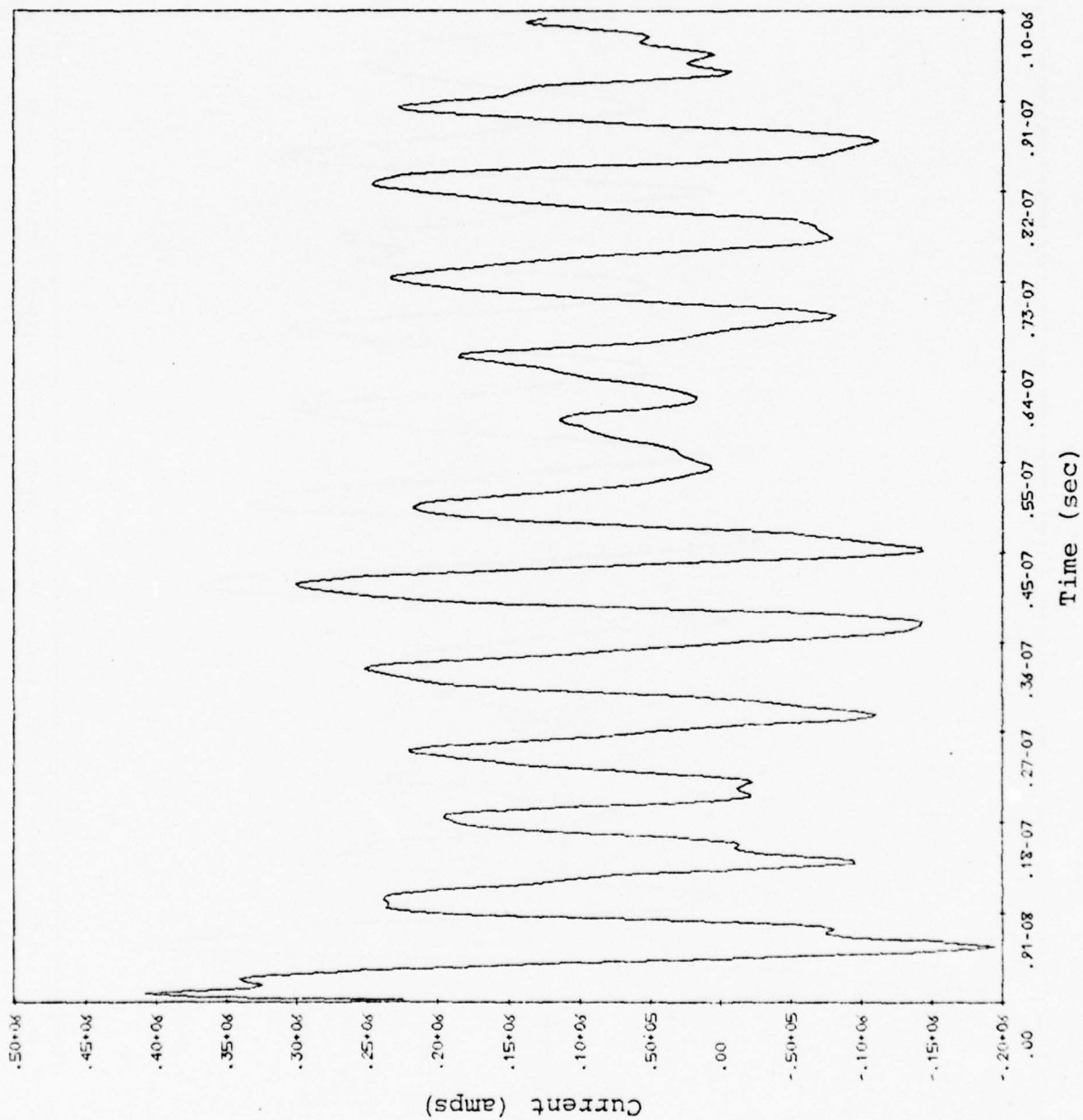


Figure 21 - Current on an isolated 120 cm strut. Tank radius is 2.5 m.

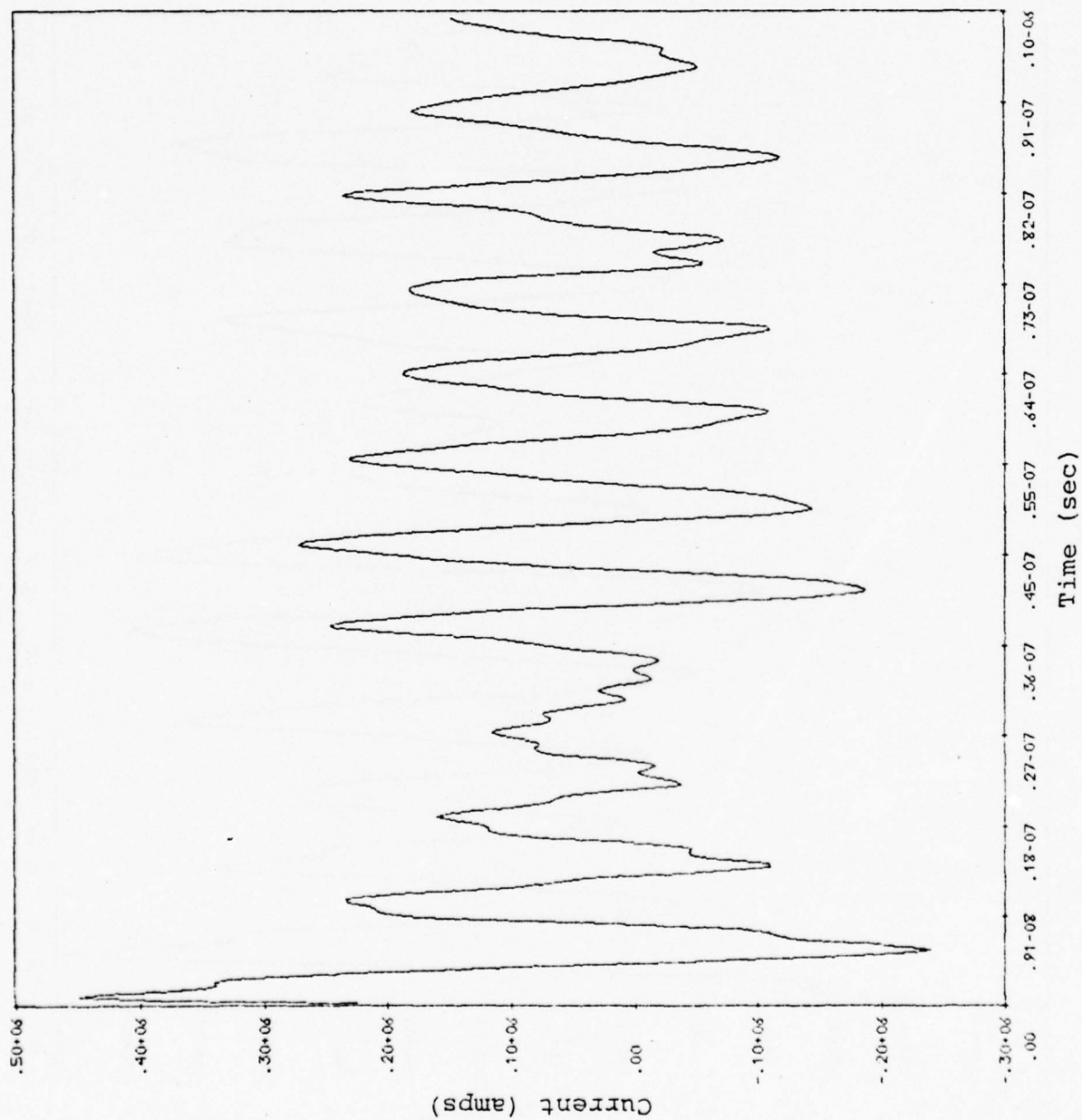


Figure 22 - Current on a 120 cm isolated strut. Tank radius is 4.5 m.

BEST AVAILABLE COPY

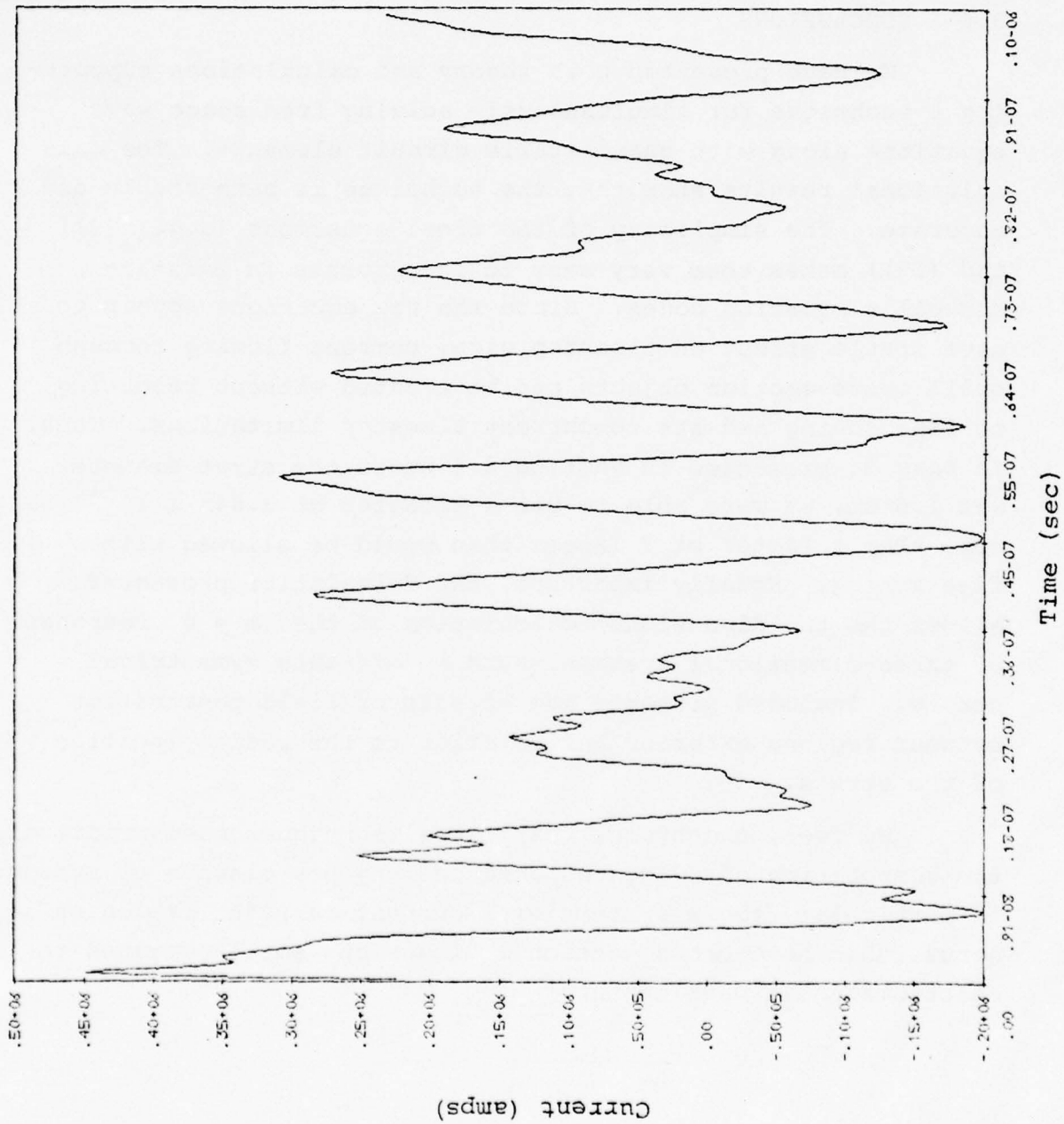


Figure 23 - Current on an isolated 160 cm strut. Tank radius is 4.5 m.



### 3.6 CONCLUSIONS

We have presented both theory and calculations supporting a technique for simultaneously solving free space wave equations along with quasi-static circuit elements. The calculational results show that the technique is both stable and accurate. The simplicity of the final equations (e.g., (21) and (22)) makes them very easy to incorporate in existing Maxwell's equation codes. Since the new equations appear to have little effect on timestep size, current flowing through small cross section objects can be treated without resorting to fine zoning and its concurrent timestep limitations. Thus, in case 2, presented in Section 3.5 where the strut diameter was 1.6 cm, we were able to use a timestep of  $3.845 \times 10^{-10}$  sec, more than a factor of 7 larger than would be allowed with fine zoning. Equally important, the formulation presented allows the two-dimensional calculation of the  $m = 0$  response of three-dimensional systems, such as off-axis symmetrical struts. Included properly are effects of field penetration between regions exterior and interior to the radial location of the struts.

We feel, therefore, that these techniques make practical the computation of SGEMP response on many new classes of systems, in particular, those systems with current-carrying cables or struts that have cross sectional dimensions small compared to electromagnetic wavelengths.

## SECTION IV

### NONREFLECTIVE FREE SPACE BOUNDARY CONDITIONS FOR SGEMP CODES

The grid in SGEMP codes is only of finite extent. For most SGEMP calculations that have been carried out, the light transit time across the grid is short; that is, comparable to the driving pulsewidth. If waves are back-scattered or reflected from the edge of the grid, they can interact with fields and currents in the emitting region. For a satellite in free space, the "clear time" for reflections should be long compared to the characteristic times associated with the driving pulse so that back-scattered waves do not enter into the calculated response. So, in order to calculate SGEMP response properly, it is necessary to devise boundary conditions which do not reflect electromagnetic waves.

One technique which has been used is to impose a multipole outgoing wave boundary condition. That is, the fields on the outermost edge are varied as if the fields in their neighboring cells were outgoing spherical waves. In general practice, only the lowest multipoles are included. While, conceptually, this technique is appropriate, in actual use it has some flaws.

One difficulty is that in order to use only the low order multipole terms, the boundaries should be a large distance (compared to object dimensions) from the radiation source. This requires either a large number of zones or large zones nearer the boundary. A second difficulty is that the waves generated numerically do not all have phase and group velocity,  $c$ , which is independent of wave number. This is especially true for wavelengths comparable to a few times the grid spacing. As a result, especially if the grid spacing is made large near the outer boundary, there will be phase mismatching on the boundary. A third difficulty concerns the cumulative effects of errors. Since the procedure is to generate fields at the boundary which

exactly cancel reflected wave amplitudes, any phase error results in both the reflected wave not being cancelled as well as a new incoming wave being generated. As a result, those modes whose reflections are not eliminated well can be pumped by the boundary conditions leading possibly to unstable numerics.

Our approach to the nonreflecting boundary problem has been to try amplitude damping as opposed to phase matching. The reasoning behind this is rather transparent; even if one does not damp a wave completely, at least one can avoid pumping the mode.

If the region of space is current free, then the two curl equations of Maxwell's equations can be written

$$\frac{\partial \tilde{E}}{\partial t} = + c \tilde{\nabla} \times \tilde{B} \quad (30)$$

$$\frac{\partial \tilde{B}}{\partial t} = - c \tilde{\nabla} \times \tilde{E} \quad (31)$$

Adding a damping coefficient,  $\nu$ , to each equation, we get

$$\frac{\partial \tilde{E}}{\partial t} = c \tilde{\nabla} \times \tilde{B} - \nu \tilde{E} \quad (32)$$

$$\frac{\partial \tilde{B}}{\partial t} = - c \tilde{\nabla} \times \tilde{E} - \nu \tilde{B} \quad (33)$$

If the spatial dependence of  $\nu$  is assumed to be extremely small, then, if  $\tilde{E}_0(\underline{x}, t)$  and  $\tilde{B}_0(\underline{x}, t)$  are solutions to Equations (30) and (31), the solutions to Equations (32) and (33) can be written as

$$\tilde{E}(\tilde{x}, t) = \tilde{E}_0(\tilde{x}, t) e^{-\nu t}$$

$$\tilde{B}(\tilde{x}, t) = \tilde{B}_0(\tilde{x}, t) e^{-\nu t}$$

As a result, waves in such a damped region would decay in time.

Finite difference equations corresponding to Equations (32) and (33) are

$$\begin{aligned} \tilde{E}^{t+1} - \tilde{E}^t &= \Delta t (c \nabla \times \tilde{B} - \nu \tilde{E})^{t+1/2} \\ &= c \Delta t \nabla \times \tilde{B}^{t+1/2} - \nu \Delta t \left( \frac{\tilde{E}^{t+1} + \tilde{E}^t}{2} \right) \\ \tilde{E}^{t+1} &= \frac{\left(1 - \frac{\nu \Delta t}{2}\right) \tilde{E}^t + c \Delta t \nabla \times \tilde{B}^{t+1/2}}{\left(1 + \frac{\nu \Delta t}{2}\right)} \end{aligned} \quad (34)$$

$$\tilde{B}^{t+1/2} = \frac{\left(1 - \frac{\nu \Delta t}{2}\right) \tilde{B}^{t-1/2} - c \Delta t \nabla \times \tilde{E}^t}{\left(1 + \frac{\nu \Delta t}{2}\right)} \quad (35)$$

Time centering is preserved and a degree of implicitness is introduced which makes the equations stable. In practice,  $\nu$  is a function of position and is only nonzero very close to the outside of the mesh.

In the following section are analytical results describing the damping and reflection of waves obeying Equations (32) through



(34) for both continuum and discrete cases. We present the results of a series of one-dimensional numerical calculations performed to determine the optimal spatial variation of the damping factor,  $\nu$ , in Section 4.2. The last section shows the effectiveness of this technique in preventing reflected waves in a two-dimensional calculation.

#### 4.1 ANALYTICAL RESULTS

It is instructive to analyze the steady oscillations corresponding to Equations (32) and (33) and to their discrete analogues, Equations (34) and (35), for a one-dimensional infinite medium with  $v > 0$  in the half space  $x > x_0$  and vanishing in the space  $x < x_0$ .

Assuming a steady wave propagating in the positive  $x$ -direction for  $x > x_0$ , we shall determine the relative amplitudes of left and right going waves in  $x < x_0$ .

For the continuous case, the substitution

$$E(x,t) = \epsilon(x,t) \cosh \tau - \beta(x,t) \sinh \tau \quad (36)$$

$$B(x,t) = \beta(x,t) \cosh \tau - \epsilon(x,t) \sinh \tau \quad (37)$$

where

$$\tau = \int_{x_0}^x v(x') dx' \quad (38)$$

reduces Equations (32) and (33) to

$$\begin{aligned} \frac{\partial \epsilon}{\partial t} &= -c \frac{\partial \beta}{\partial x} \\ \frac{\partial \beta}{\partial t} &= -c \frac{\partial \epsilon}{\partial x} \end{aligned} \quad (39)$$

equations which are formally equivalent to the original Maxwell equations without the damping term.

Equations (39) admit a steady wave propagating to the right

$$\begin{aligned}\epsilon &= \epsilon_0 e^{i(\omega t - kx)} \\ \beta &= \epsilon_0 e^{i(\omega t - kx)} = \epsilon\end{aligned}\quad (40)$$

with

$$\omega = ck \quad (41)$$

Thus,

$$E = B = \epsilon e^{-\tau} \quad (42)$$

also propagates to the right. The  $E$  and  $B$  fields are damped in  $x > x_0$ ; in  $x < x_0$ , the fields have their free space values and there is no reflected wave.

In the discrete case, the waves may also be damped in  $x > x_0$ ; but, in general, there will exist a reflected wave in the half space  $x < x_0$ . Now assume that  $v = \text{constant}$  for  $x > x_0$ , i.e., for the discrete spatial coordinate  $n \geq N$ , and vanishes otherwise.

Assuming a solution of the form

$$\begin{aligned}E &= E_0 e^{i(j\omega\Delta t - nk'\Delta x)} \\ B &= B_0 e^{i[(j+1/2)\omega\Delta t - (n+1/2)k'\Delta x]}\end{aligned}\quad (43)$$

Equations (34) and (35) reduce to

$$\left( \frac{2i \sin \frac{\omega\Delta t}{2}}{\Delta t} + v \cos \frac{\omega\Delta t}{2} \right) B_0 = \frac{2i c \sin \frac{k'\Delta x}{2}}{\Delta x} E_0 \quad (44)$$

$$\left( \frac{2i \sin \frac{\omega\Delta t}{2}}{\Delta t} + v \cos \frac{\omega\Delta t}{2} \right) E_0 = \frac{2i c \sin \frac{k'\Delta x}{2}}{\Delta x} B_0 \quad (45)$$

where  $E_0 = \pm B_0$ ; in particular, for  $E_0 = B_0$

$$\begin{aligned}\sin \frac{k'\Delta x}{2} &= \frac{\Delta x}{c\Delta t} \sin \frac{\omega\Delta t}{2} - i \frac{v\Delta x}{2c} \cos \frac{\omega\Delta t}{2} \\ &= \sin \frac{k\Delta x}{2} - i \frac{v\Delta x}{2c} \cos \frac{\omega\Delta t}{2}\end{aligned}\quad (46)$$

where

$$\sin \frac{k\Delta x}{2} = \frac{\Delta x}{c\Delta t} \sin \frac{\omega\Delta t}{2} \quad (47)$$

is the dispersion relation in the absorption-free half space.

The imaginary part of  $k'$  determines the attenuation in the absorbing medium. Writing  $k'\frac{\Delta x}{2} = U_R + iU_I$ , and separating real and imaginary parts in Equation (46), there results

$$\begin{aligned}\cosh U_I \sin U_R &= \sin \frac{k\Delta x}{2} \\ \sinh U_I \cos U_R &= - \frac{v\Delta x}{2c} \cos \frac{\omega\Delta t}{2}\end{aligned}$$

By inspection, we find

$$U_I < 0 \quad \text{for} \quad \frac{k\Delta x}{2} \leq \frac{\pi}{2}$$

and

$$\frac{c\Delta t}{\Delta x} < 1$$

Thus, all wavelengths resolvable on the mesh are damped; wavelengths near  $\lambda = 2\Delta x$  are only weakly damped for  $\frac{c\Delta t}{\Delta x}$  near unity and are undamped for  $\frac{c\Delta t}{\Delta x} = 1$ .

To obtain the reflection coefficient, consider solutions having the form of Equation (43) with  $B_0 = E_0$  for  $n \geq N$ , and the form



$$E = e^{ij\omega\Delta t} (ae^{-ikn\Delta x} + be^{ikn\Delta x})$$

$$B = e^{i(j+1/2)\omega\Delta t} (ae^{-ik(n+1/2)\Delta x} - be^{ik(n+1/2)\Delta x})$$

for  $n \leq N-1$ .

Equations (43) determine  $E_N$  and  $B_{N+1/2}$ . The complex coefficients  $a$  and  $b$  are determined using Equation (34) for  $n = N$  and Equation (35) for  $n = N-1$ , remembering that  $v_N = v$  and  $v_{N-1} = 0$ . Following a simple but tedious calculation, we find the reflection coefficient

$$r = \left| \frac{b}{a} \right| = \left| \frac{1 - e^{-i(k'-k)\frac{\Delta x}{2}}}{1 + e^{-i(k'+k)\frac{\Delta x}{2}}} \right|$$

where the complex wave number  $k'$  is related to the given real quantities  $k$  and  $v$  by Equation (46).

In general, although Equation (46) must be solved numerically before  $r$  can be determined, two limiting cases are amenable to simple analysis. When

$$k \frac{\Delta x}{2} \ll 1$$

$$\frac{v\Delta x}{2c} \ll 1$$

and

$$\frac{c\Delta t}{\Delta x} \leq 1$$

then

$$r \approx \frac{v\Delta x}{2c}$$

For  $\frac{c\Delta t}{\Delta x} = 1$  and  $k\Delta x = \pi$ ,  $r = 0$ . Nevertheless, since  $k' = 0$ , a wave encountering a boundary at finite  $x$  in the damping medium will be reflected and return with undamped amplitude

to the absorption free region. In practice, however,  $\frac{c\Delta t}{\Delta x} < 1$ , and there will be some damping of the reflected wave, the amount depending on the thickness of the absorbing medium.

#### 4.2 1-D PARAMETER STUDY

The spatial variation of the damping coefficient,  $\nu$ , in Equations (32) and (33) makes the problem of analytically predicting wave behavior difficult since the space is no longer homogeneous. As a preliminary indication of the method's validity, a one-dimensional transverse electromagnetic wave code was written. This code has 100 cells in the x-direction with edge centered y-components of electric field and cell centered z-components of the magnetic field. It numerically follows the propagation of plane polarized TEM modes in the x-direction. The wave source was a sinusoidally varying y-component current located at the midpoint of the grid. The damping coefficient,  $\nu$ , was zero everywhere except within a specified number of cells from either edge of the mesh. Calculations were run to determine the functional form of the damping coefficient's spatial dependence which best minimizes the amplitude of the reflected wave after the wave source was turned off (50 cycles).

After several runs, several characteristics of the technique were apparent. The first was that increasing the number of damping zones from 5 to 10 on each side of the mesh made small differences (factors of 2) in the reflected wave amplitude. Second, the damping should increase slowly from zero to some number such that

$$\nu \Delta t > 1.0$$

Finally, the damping effectiveness was proportional to wavelength.

Let us examine the results of a set of runs made with

$$\left( \frac{\nu(x) \Delta t}{2} \right)_{\max} = 3.8. \quad \text{The damping increases quadratically from zero in each boundary region}$$

$$\frac{\nu(x)\Delta t}{2} = \begin{cases} 3.8*(5-x)^2/25, & x < 5 \\ 0, & 5 \leq x \leq 95 \\ 3.8(x-95)^2/25, & x > 95 \end{cases}$$

Table 1 presents the maximum electric field amplitude in the mesh after 200 timesteps ( $c\Delta t = 0.90$ ) for a range of pump frequencies. It is apparent that longer wavelengths damp most effectively, as discussed in Section 4.1, but that even for high frequency, short wavelengths, over 93 percent of the wave amplitude is damped after 200 cycles. The damping of the longest wavelength is almost 99 percent effective. Figure 24 shows a plot of the percent remaining after 200 cycles vs. the frequency of the pump mode. The relation is linear to a remarkable degree. This bodes extremely well for SGEMP response calculations, since the wavelengths associated with the strong electromagnetic waves generated by the ringing of surface currents are usually large compared to grid spacings.

One point to note is that the damping coefficient gets considerably larger than the timestep, that is,

$$\nu\Delta t > 1$$



Table 1  
THE EFFECTIVENESS OF THE DAMPING  
ON WAVES FOR VARIOUS FREQUENCIES

| $1/\omega\Delta t$ | $ B(t=50) _{\max}$ | $ B(t=200) _{\max}$ | % remaining |
|--------------------|--------------------|---------------------|-------------|
| 10                 | 0.550              | 0.037               | 6.7         |
| 15                 | 0.556              | 0.024               | 4.3         |
| 20                 | 0.521              | 0.018               | 3.5         |
| 30                 | 0.511              | 0.012               | 2.3         |
| 60                 | 0.504              | 0.006               | 1.2         |

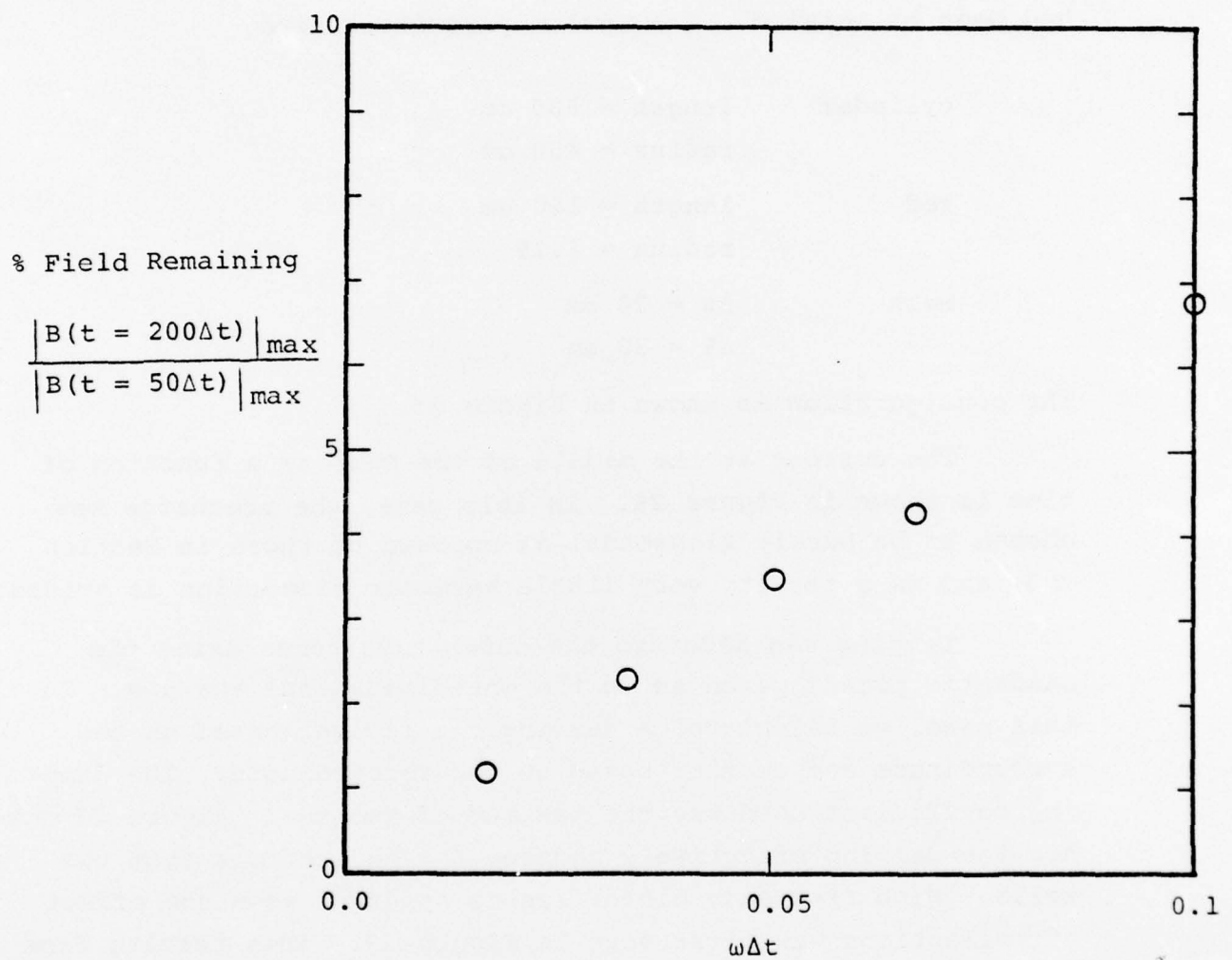


Figure 24 - Remaining field amplitude vs. frequency for the 1-dimension parameter study.

#### 4.3 DAMPED WAVE BOUNDARIES IN TWO-DIMENSIONS

To test the usefulness of the damping theory in two dimensions, a sample calculation was performed. Previously, the behavior of a precharged rod inside a conducting cylinder had been calculated. The system parameters were

|          |                      |
|----------|----------------------|
| cylinder | length = 600 cm      |
|          | radius = 450 cm      |
| rod      | length = 120 cm      |
|          | radius = 1.19        |
| mesh     | $\Delta z = 20$ cm   |
|          | $\Delta R = 30$ cm . |

The configuration is shown in Figure 25.

The current at the middle of the wire as a function of time is shown in Figure 26. In this case, the precharge was chosen to be purely sinusoidal as opposed to those in Section 3.5, and as a result, very little harmonic distortion is evident.

Damping was added to the outer time zones using the quadratic prescription as in the one-dimensional example. In this case, we calculated a damping coefficient based on the  $z$ -coordinate and another based on the  $r$ -coordinate. The damping coefficient used was the maximum of the two. Figure 27 shows how the damping effectively reduced the reflections from the walls. High frequency distortion is apparent when the effect of reflections was first seen in Figure 27. This results from the inefficient damping of high frequency modes as discussed in the previous sections. The overall stability of the system should be noted; there are no growing oscillations at late times.

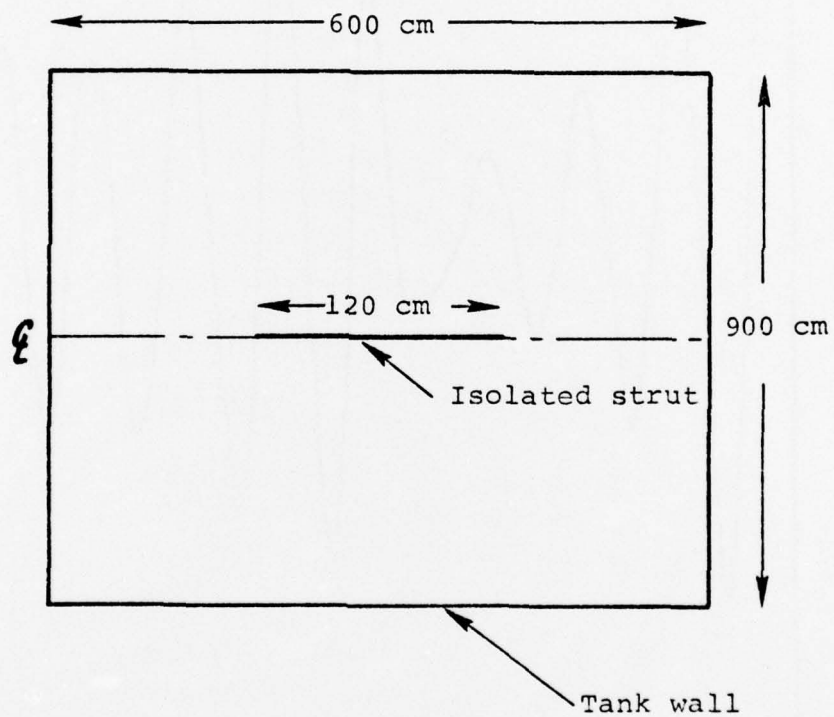


Figure 25 - The configuration used for testing the effectiveness of the damping in two-dimensions.



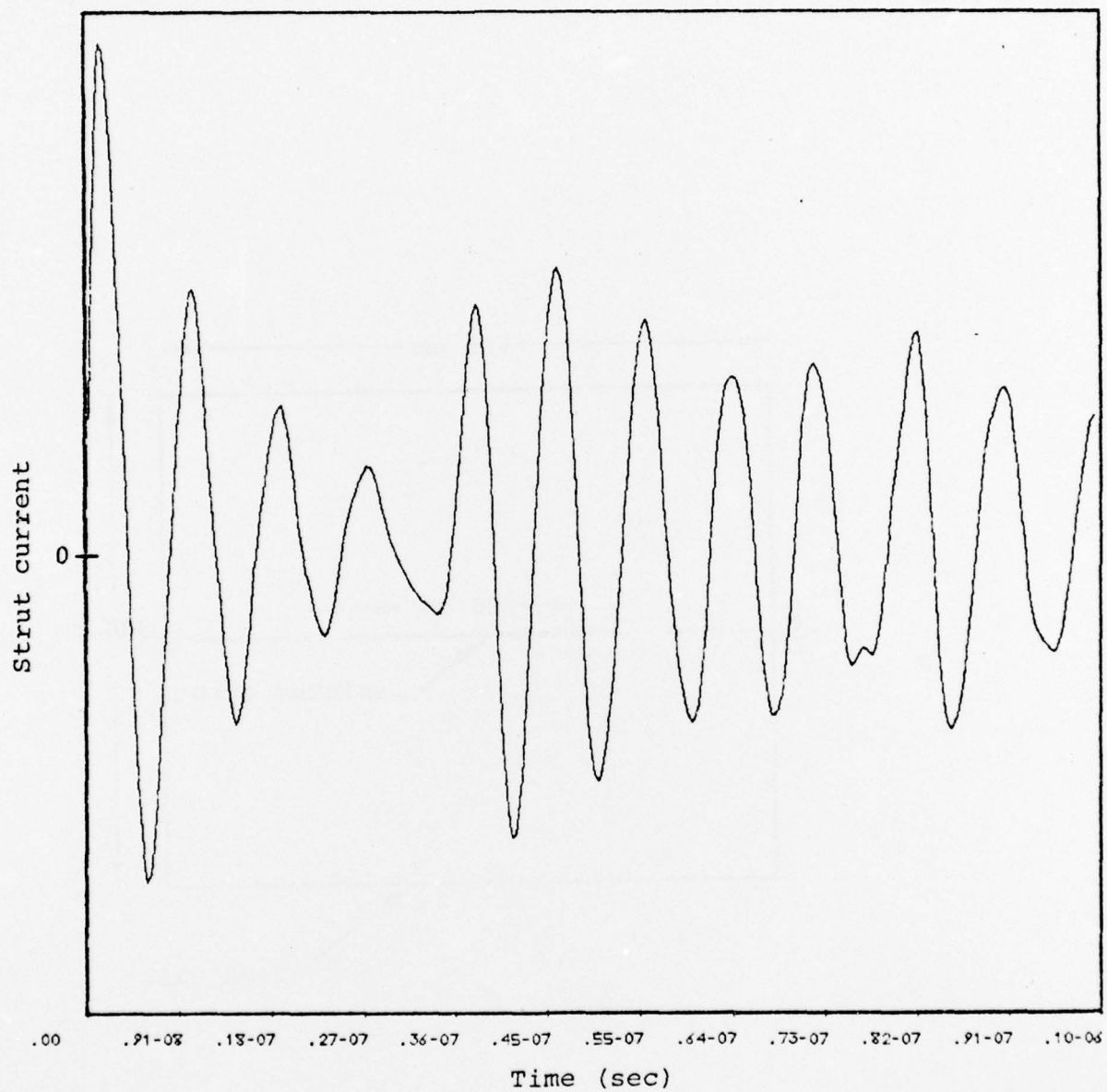


Figure 26 - The current at the wire center vs. time for the case with no damping.

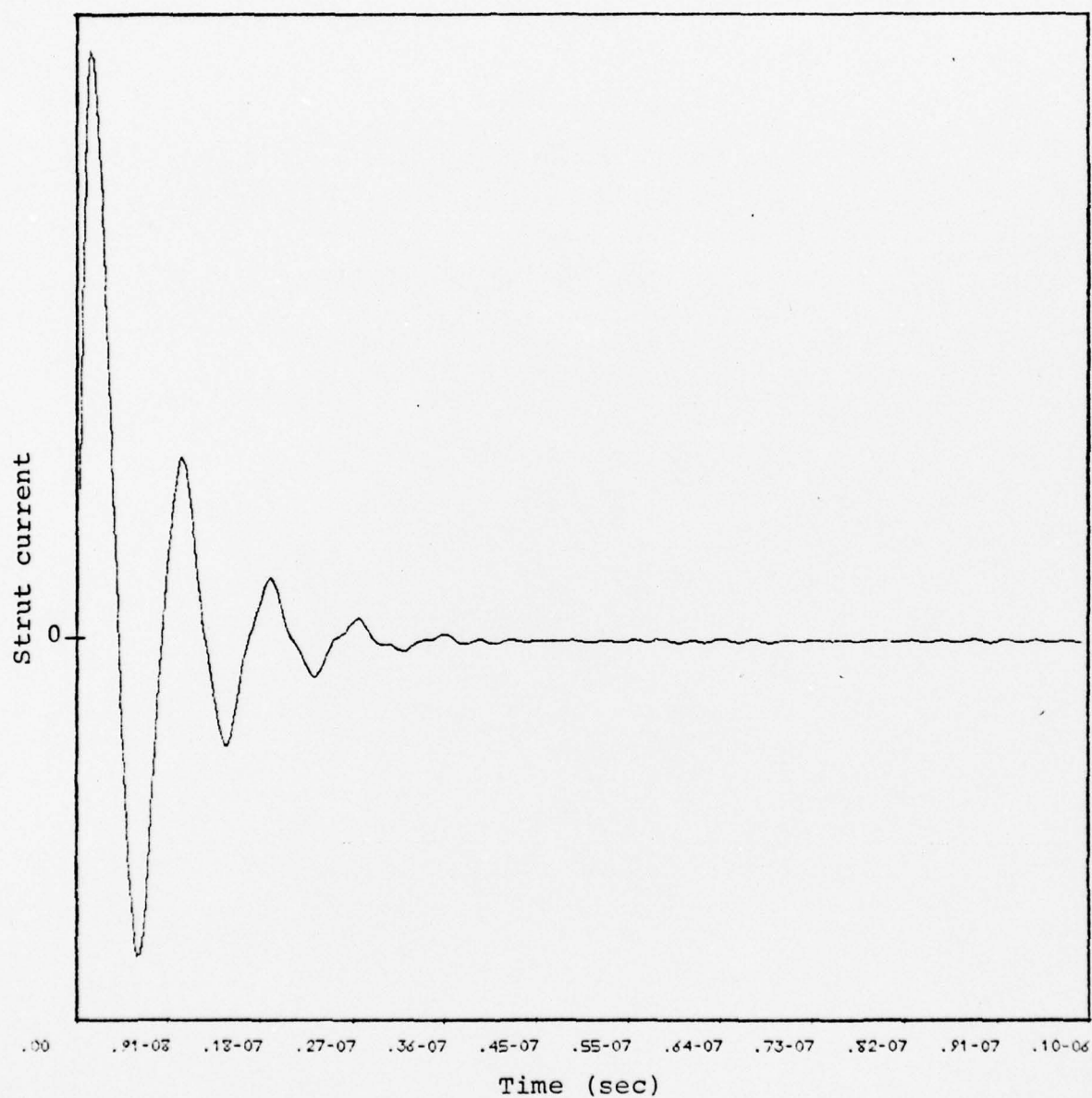


Figure 27 - The current at the wire center vs.time with damping in the outermost 5 zones. The damping parameters were chosen from the results of the 1-D study described in Section 4.2.